The effect of strain on the crystallinity of carbonaceous matter: Application of Raman spectroscopy to deformation experiments

Benjamin Moris-Muttoni, Hugues Raimbourg, Rémi Champallier, Romain Augier, Abdeltif Lahfid, Emmanuel Le Trong, Ida Di Carlo

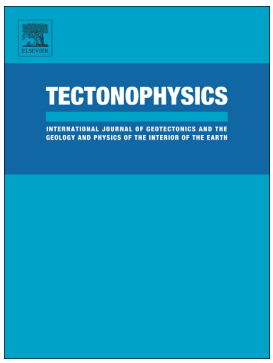

The effect of strain on the crystallinity of carbonaceous matter: Application of Raman spectroscopy to deformation experiments

Benjamin Moris-Muttoni, Hugues Raimbourg, Rémi Champallier, Romain Augier, Abdeltif Lahfid, Emmanuel Le Trong, Ida Di Carlo

PII: S0040-1951(23)00424-9

DOI: https://doi.org/10.1016/j.tecto.2023.230126

Reference: TECTO 230126

To appear in: *Tectonophysics*

Received date: 14 April 2023

Revised date: 8 November 2023

Accepted date: 10 November 2023

Please cite this article as: B. Moris-Muttoni, H. Raimbourg, R. Champallier, et al., The effect of strain on the crystallinity of carbonaceous matter: Application of Raman spectroscopy to deformation experiments, *Tectonophysics* (2023), https://doi.org/10.1016/j.tecto.2023.230126

The effect of strain on the crystallinity of carbonaceous matter: application of Raman spectroscopy to deformation experiments

Benjamin Moris-Muttoni[a*], Hugues Raimbourg[a], Rémi Champallier[a], Romain Augier[a], Abdeltif Lahfid[b], Emmanuel Le Trong[a], Ida Di Carlo[a]

[a] Institut des Sciences de la Terre d'Orléans (ISTO), Université d'Orléans, CNRS, BRGM, ISTO, UMR 7327, F-45071, Orléans, France.

[b] Bureau de recherches géologiques et minières (BRGM), F-45060, Orléans, France.

[*] **Corresponding authors: Hugues Raimbourg at ISTO, univ. d'Orléans, UMR7327, Orléans, France, hugues.raimbourg@univ-orleans.fr**

0-Abstract

Raman spectroscopy, applied to the carbonaceous matter (CM) present in fault zones, is a potentially powerful tool to aid in the reconstruction of slip conditions, provided the respective effect of heating and strain can be disentangled. For this purpose, we have carried out static heating and deformation experiments on low-grade sediments containing disseminated CM particles and tracked the evolution of CM crystalline ordering (crystallinity) using Raman spectroscopy. Heating at high pressure (200 MPa) at varying temperatures (500 to 800°C) and durations (3 to 1080h) resulted in an increased crystallinity, which was observed by an increase in the intensity ratio of the Disordered Band over the Graphite Band (Intensity Ratio R1 parameter) of the Raman spectra. The experimental relationship between R1, T and duration was compiled into a law of evolution, which was then used to design the deformation experiments. Experiments were performed in a Paterson rig at 150 MPa or in a Griggs-type rig at 1 GPa. We observed two types of deformation microstructures: (1) purely brittle ones, such as breccia along slip planes and (2) ductile ones, such as foliated layers, resulting from grain reorientation and comminution along with dissolution precipitation. In all deformation microstructures, an increase in R1 is visible and interpreted to be the result of higher crystallinity of carbonaceous particles. Such increase is negligible in breccia, but is significant, up to 40%, in ductile deformation zones. The slow strain rates prevailing in ductile deformation prevented any local temperature increase, therefore the increase in crystallinity of the CM can be solely attributed to deformation. Thus, in natural fault zone, the increased crystallinity of CM reported in the literature and interpreted to be the result of frictional heating during earthquakes might rather be the result of strain localization without transient temperature increase.

1-Introduction

Determining the degree of crystallinity of the carbonaceous material is possible through Raman Spectroscopy of Carbonaceous Matter (RSCM) analyses. Upon heating, the degree of crystallinity increases by thermal maturation through the carbonization (low-grade to greenschist-facies metamorphism) and graphitization stages (amphibolite- to granulite-facies metamorphism) (Beyssac et al., 2002; Lahfid et al., 2010; Oberlin, 1984). Qualitative correlations first linked the degree of metamorphism to CM lattice organization (Pasteris and Wopenka, 1991; Wada et al., 1994). More recently, quantitative calibration of these correlations resulted into the development of geothermometers based on the RSCM parameters, which are applicable to a temperature range of 150 to 650°C (Aoya et al., 2010; Beyssac et al., 2002; Kouketsu et al., 2014; Lahfid et al., 2010; Rahl et al., 2005). These geothermometers are widely used in ancient subduction and collisions zones studies (Beaudoin et al., 2015; Clerc et al., 2015; Lanari et al., 2012).

Amongst regional-scale temperature trends, anomalous RSCM spectra, i.e. these strongly deviating from the trend, are sometimes observed (Kedar et al., 2020; Barzoi, 2015; Barzoi and Guy, 2002; Moris-Muttoni et al., 2022). For example, the ratio of the two main peaks of the Raman signal is increased by up to 40% in fault zones from the Shimanto Belt (Moris-Muttoni et al., 2022) and by ~20% in a high strain zone in the overturned limb of a fold in the Alps (Kedar et al., 2020). A possible interpretation of these anomalies involves the effect of strain, which was mainly studied on well-crystallized CM in the advanced graphitization processes of natural (Kedar et al., 2020; Nakamura et al., 2015; Suchy et al., 1997) or experimental (Bonijoly et al., 1982; Bustin et al., 1995; Ross et al., 1992; Ross and Bustin, 1990) samples. An additional explanation for these anomalies relies on transient and local heating, caused by frictional slip during earthquakes (Furuichi et al., 2015; Ito et al., 2017; Ujiie et al., 2021). The case of anomalous RSCM signals in fault zones is particularly problematic, as they potentially combine the contribution of both strain and transient heating to CM crystallinity (Figure 1).

To explore the respective effects of heating and strain on CM crystallinity in low-grade samples, i.e. conditions of metamorphism at or below 300-350°C, we have carried out static heating experiments, in

order (1) to determine the relevant Raman spectra features that can be used to track crystallinity changes with heating, (2) to define the kinetic law that connects such features to temperature and time and (3) to define the appropriate conditions for deformation experiments that constitute the other part of the present work. These deformation experiments were exploratory, so rather than a systematic parametric study over a narrow domain of conditions, we considered a large range of experimental conditions and geometries. In particular, we used two different apparatuses, the Paterson rig and the Griggs-type rigs, enabling a large range of conditions of confining pressure to be explored. These experimental conditions led to a variety of microstructures, which were then systematically analyzed by RSCM in order to connect deformation processes with CM evolution.

2-Starting material and Methods

2.1 Starting material

Samples used for static heating in autoclaves and deformation experiments have been selected from the Shimanto Belt, on the island of Kyushu in Japan, where the first-order thermal structure across the belt (over ~100km width) has already been studied by RSCM (Raimbourg et al., 2014; Raimbourg et al., 2017; Raimbourg et al., 2019). Two homogeneous shales, belonging to turbidites formations, have been sampled and used as starting material. The choice of shales was motivated by the fact that this material contains relatively abundant particles of carbonaceous matter (Raimbourg et al., 2017) and Raman spectra anomalies detected in fault zones were often found in shale-rich host rock (e.g., Ujiie and Kimura, 2014, Meneghini et al., 2010).

The maturity of the carbonaceous particles in the starting materials has been investigated using RSCM, vitrinite reflectance (%VR) and RockEval pyrolysis (all methods, except for RSCM, which is described below, are presented in the Supplementary Materials S2). Chemical and mineralogical compositions of the whole rock have been obtained by X-ray fluorescence (XRF) and diffraction (XRD) analyses, respectively. Microscopy techniques have not been used due to the small size of particles in both samples.

The first starting material, 18NOB01A, is from very low-grade metamorphic turbidites in the Miyazaki Group in the Shimanto Belt (Supplementary Materials S2). The Miyazaki Group is a Pliocene forearc basin composed of a thick sequence of turbidites (Murata, 1997; Shuto, 1961). The selected material has been sampled from a layer of shale in the turbidite unit and is composed of a fine assemblage of Quartz – Albite – K-feldspar – Calcite – Mullite – Illite – Pyrite. Semi-quantitative estimation based on the Rietveld method shows that the majority of minerals present are Quartz and Albite (ca. 60%), whereas calcite represents about 5% of the rock and the rest is composed of clays (ca. 35%). Average vitrinite reflectance values obtained for 18NOB01A is 0.54 ± 0.04% and corresponds to a temperature of 84 ± 7 °C based on the calibration of Barker (1988) (Table 1) and a thermal maturity between the end of the diagenesis and the beginning of the catagenesis. RSCM parameters have been measured but the evolution of the Raman parameters at these low degrees of maturity is still controversial.

The second starting material, HN78, comes from turbidites belonging to the Hyuga Coherent unit in the Shimanto Belt, which was buried and deformed within the accretionary wedge. The selected material was sampled from a layer of shale within turbidites. It is very similar in terms of lithology to 18NOB01A but is considered to be a higher metamorphic grade. This sample is composed approximately of 45% Quartz – 18% Albite – 33% Illite – 5% Chlorite based on the XRD results and the semi-quantitative Rietveld method. The chemical composition is given in Table 1. In this sample, the CM has reached a thermal maturity at the transition between the metagenesis and the metamorphism. The calculated temperature obtained using the RSCM calibration of Lahfid et al. (2010) is approximately 201 ± 11°C. No vitrinite reflectance could be measured.

From RockEval pyrolysis, the carbonaceous particles in both 18NOB01A and HN78 belong to Type III, i.e., originate from small debris of terrestrial plants.

2.2 Analytical methods

2.2.1 RSCM

Raman Spectroscopy of Carbonaceous Matter (RSCM) has been used to constrain the crystallinity of the carbonaceous material (CM) present as micron-size particles disseminated in the rock samples. Analyses were carried out using the ReniShaw InVIA microspectrometer, at ISTO-BRGM, Orléans, using an argon laser beam of 514 nm focused on the sample by a DM2500 Leica microscope equipped with x100 objective. These apparatuses are coupled with Renishaw software Wire 4.0. Acquisition time was 30 to 200 seconds (spectrometer opening time was ~5 s with 40 spectra accumulation). Laser power was maintained at less than 0.5 mW on the surface of the sample to avoid heating of CM grain during analyses. To avoid defect bands generated during thin section polishing all analyses were performed on subsurface grains by focusing the laser beam through transparent or translucent minerals (Ammar and Rouzaud, 2012; Katagiri et al., 1988; Pasteris, 1989). For the static heating experiments, around 20 particles have been measured on each sample in order to calculate average Raman parameters. For the deformation experiments, each particle is spatially located and associated with a deformation microstructure, so that variations across the sample or across the different microstructures can be determined.

Raman spectra processing was done using PeakFit v4.12. To carry out the linear baseline correction, the baseline fit was obtained by selecting the data points in the ranges 900-1000 and 1900-2000cm^{-1}. The Raman spectra of the CM considered here is composed of two maxima, one around 1600cm^{-1} (the graphite-like "G band"), corresponding to highly-ordered carbon and one around 1350cm^{-1} (the defect "D band"), corresponding to disordered carbon (Beny-Bassez and Rouzaud, 1985; Lahfid et al., 2010; Sadezky et al., 2005; Tuinstra and Koenig, 1970; Wang et al., 1990).

To interpret Raman spectra, several parameters were assessed. First, on baseline-subtracted spectra, the position and intensities of the two maxima (the D and G bands) were determined. Second, we applied peak deconvolution procedure to the baseline-subtracted spectra, following Lahfid et al. (2010). This approach is well adapted to low metamorphic grade material and consists of a 5 band

(D1, D2, D3, D4 and G) deconvolution using Lorentzian functions. D4+D1+D3 peaks form the D band, while the G band is composed of D2 + G peaks.

During the transformation from low-grade carbonaceous matter to perfect graphite, Raman spectra evolution can be decomposed in two successive steps. In the low temperature realm (i.e. 200-330°C), the D band increases in area and intensity with increasing metamorphic grade (Lahfid et al., 2010), while at higher temperature, the D band decreases in area and intensity with increasing grade (Beyssac et al., 2002). In the present study, parameters used to track the CM evolution during static heating and deformation experiments are the D- and G-band positions, full width at half maximum of the D1 and G bands (FWHM), R1 intensity ratio (Beyssac et al., 2002) and distance between the D and G bands (i.e. RBS in Henry et al. (2019)). Of particular interest in the present work is the evolution of R1 (Figure 4), as it shows anomalies in experimentally and naturally faulted rocks (Muirhead et al., 2021), which still remains to be understood. In addition, peak area ratios used for thermometric calibrations (Beyssac et al., 2002; Lahfid et al., 2010), resulting from peak deconvolution, have also been analyzed.

All raw and processed Raman spectra are available at https://doi.org/10.5281/zenodo.8321278.

2.2.2 Electron microscopic imaging

At ISTO, Orléans, Scanning Electron Microscopy (SEM) analyses were performed by using a SEM Merlin Compact Zeiss, equipped with an EDS Bruker Quantax detectors, at 15kV. EDS maps were acquired at 15kV with a dwell time of 850µs and summed over 9 scans.

2.3 Experiments

2.3.1 Hydrostatic heating experiments

Hydrostatic thermal maturation has been performed in autoclaves in order to understand the CM evolution under constant temperature and pressure during the carbonization and early graphitization stages. Powdered samples of the two shales, 18NOB01A and HN78, sealed in gold capsules, were matured at a pressure 150MPa and a temperature of 500 to 800°C for a duration between 3 hours to 45 days. The heating rate was set at 4.5°C/min. Additionally, distilled water was added to some

experiments. The details of the sample preparation and experimental techniques are presented in Supplementary Materials S1. After completion of the experiments, the CM crystallinity was estimated by RSCM analyses. All the results obtained are presented in Table 2.

2.3.2 Deformation experiments

2.3.2.1 Objectives and overview: This study includes 8 Paterson Rig apparatus and 4 solid-medium Griggs apparatus experiments (Figure 1, Figure 2), performed at low (150MPa) and high (1GPa) confining pressures, respectively. The aim of these experiments is to reproduce experimentally the structures of deformations shown in Figure 1, i.e. faults with features of brittle deformation (such as fault core gouge) coexisting with more distributed, ductile, deformation structures (such as the progressively elongated clasts), as well as to analyze the corresponding Raman signatures. For this purpose, we explored experimental conditions wherein (1) both brittle and ductile deformation microstructures could be observed and (2) contrasting Raman features are observed, enabling the effect of deformation on CM crystallinity to be determined.

Laboratory rates of deformation are by definition orders of magnitude larger than natural ones; therefore, to compensate for this, large (typically >700°C) experimental temperatures are necessary in order to avoid purely brittle deformation and to reach the onset of ductile deformation. However, during deformation and static heating experiments (see the section 4.1) at high temperatures (700 or 800°C), the CM Raman spectra tends asymptotically towards an endmember shape, which corresponds to the end of the carbonization processes, such that the effect of deformation vanishes.

As a result of this delicate compromise to obtain simultaneously a large variety in microstructures and contrasting Raman signature across the experimental sample, a large range of conditions were tested on two distinct deformation apparatuses. In many instances, deformation behavior was mostly brittle and deformation was extremely localized on slip planes.

With Paterson Rig apparatus, 5 experiments were carried out in simple shear geometry and 3 in co-axial mode on cylinders. With the Griggs apparatus, 2 experiments have been carried out at constant deformation rates in the “Tullis-modified” Griggs apparatus and 2 in the new Griggs apparatus at

constant external load. Deformation experiments were performed on intact or powdered shale 18NOB01A. Experimental conditions are detailed in Table 3.

2.3.2.2 Experimental procedure in the Paterson rig: The deformation experiments were carried out on the Paterson rig available at Orléans (see details in Paterson (1990) and Figure 2). The confining pressure was applied by Argon up to a pressure of 100MPa before heating. The temperature was increased to the target temperature at a rate of 4.5°C/min, after which the confining pressure is adjusted at 150 MPa. When the temperature and pressure were stable, the load-cell was run in order to begin the deformation. Deformation experiments were carried out at 150 MPa, from 600 to 700°C, for 3 to 42 hours and at constant displacement rates of 0.1 to 0.01 µm/s. One 72h experiment was conducted at a constant load, corresponding to ~$10^{-7}s^{-1}$ strain rate. At the end of the experiment, the oven was turned off and the temperature dropped below 100 °C in few minutes. At this temperature, the autoclave was then depressurized slowly to prevent decompression cracks. After the experiments, the experimental assembly was removed from the autoclave and the sample was cut and prepared for analysis.

2.3.2.3 Experimental procedure in the Griggs-type rig:

The Griggs-type deformation experiments were carried out on two different apparatuses, both present in Orléans. The Griggs-type rigs are either a Tullis-modified design (Marti et al., 2018; Pec et al., 2012) or a more recent design ("new Griggs" (Précigout et al., 2018)). The Tullis-modified rig or the new Griggs were used to perform constant strain-rate (at ~2 $10^{-5}s^{-1}$) and constant external load experiments, respectively. In the latter type of experiments, the applied nominal load is fixed, but the actual load on the sample increases with deformation as the surface of overlap of the two pistons decreases. The confining pressure was applied by either a KI or NaCl confining medium at conditions of deformation at 400°C or 600°C, respectively. The heating rates were 16°C/min for the Tullis-modified design (experiments T609BM and T610BM), and 30°C/min for the "new Griggs" (experiments OR87BM and OR92BM).

In the constant load experiments, two sets of conditions were tested. In OR87BM, the sample was left at 600°C and 1 GPa for 17 hours before deformation proceeded. Several steps of increasing load were then applied, and the strain rate for the highest external load (500 MPa) was ~$10^{-5}s^{-1}$. In OR92BM, the sample was left at 600°C and 1 GPa for 1/2 hour before setting the external load (at 500 MPa), resulting in a much higher deformation rate on the order of $5.10^{-4}s^{-1}$.

3. Results

3.1 Static heating experiments

Of all the parameters studied (Figures 3 and 4, Supplementary Materials S3), the ones that show the most significant and straightforward relationship to heating, for the different temperatures applied, are the ratios of areas of fitted peaks RA1 (Lahfid et al., 2010)-(Figure 3a), as well as the intensity ratio R1 (Figure 3b). In particular, the latter parameter follows a monotonic (i.e., $f(x)$ varies only in one direction over the interval of interest $x \in [x1, x2]$) increase in the three highest temperatures (out of the four tested ones).

3.2 Deformation experiments

3.2.1 Mechanical behaviour

Paterson experiments (Figure 5 and Table 3): In the two experiments containing porous alumina and having a connection of the powdered sample to a reservoir of water with controlled pressure (PP629 and PP630), the sample deformation only consisted of compaction, until deformation shifted to the alumina pistons. These two experiments are therefore not considered in the following. To avoid dehydrating the sample upon heating and transform of the material into hard and undeformable ceramics, all the other Paterson experiments used non-porous pistons.

In all experiments, including shear and coaxial geometries (with the exception of the constant load experiment (PP649)), stick-slip events, characterized by a sharp stress drop and rapid forward motion of the load cell, occurred (Figure 5). The differential stress before the initial stick-slip event in the coaxial experiments PP638 and PP641 is close to the Goetze criterion ($\sigma_1 - \sigma_3 = P_{conf} = 150\ MPa$),

considered as the onset of brittle deformation (Kohlstedt et al., 1995). In shear experiments, the differential stress before the initial stick-slip event is much more variable, from 60 to 130 MPa. The differential stress after stick slip is also variable, from ~30 to 70MPa.

Griggs experiments (Figure 6 and Table 3): The two, constant strain-rate experiments (T609BM and T610BM) show contrasting mechanical behavior, as a result of applied temperatures of 400 and 600°C, respectively. At 400°C (T610BM), the differential stresses increase to values of ~930 MPa, close to the Goetze criterion (1GPa), before a significant and progressive weakening down to 630 MPa. At 600°C (T609BM), the differential stresses increased monotonically throughout the experiments, while remaining at values of below 400 MPa. The loading curve in the experiment at 600°C has a much lower slope than in the experiment at 400°C.

In the constant load experiments, large differences arose as a result of the duration of the heating stage at 600°C and 1 GPa without any differential stress, which precedes the deformation stage. For a similar nominal load of 500 MPa, the experiment statically heated for 17h (OR87BM) was by a factor of ~50 more viscous than the experiment statically heated for ½ hour at the same conditions before deformation (OR92BM).

3.2.2 Microstructures

Low pressure experiments (Paterson rig):

In all shear geometry experiments, slip along the boundary between the piston and the sample was observed. In sample PP633, breccia zones, characterized by a large and heterogeneous grain size reduction, and a large porosity compared to undeformed domains, are distributed through the sample (Supplementary Material S4). In sample PP636, along the piston-sample boundary, a µm-thick layer is present, where grain size reduction proceeded down to the submicron scale and porosity has disappeared. Further away from the boundary, a ~5-10 µm thick layer is constituted of clasts of the original material, embedded in clays developing a foliation (defined by phyllosilicate preferred orientation), which asymptotically merges into the boundary layer. Further away, deformation is no longer visible.

In coaxial experiments (PP638 and PP641), conjugate fractures are observed. They consist, in both experiments, in straight slip surfaces cutting across the whole samples. In PP638, the slip plane is surrounded by breccia layers with a thickness of ~100 µm, asymmetrically developed on both sides, or localized in step-overs of the slip plane (Supplementary Material S4).

In PP641, which was deformed at a strain rate 10 times lower than PP638, a high strain, foliated layer developed along the slip plane. The foliation is defined as the preferential orientation of elongated clasts of quartz/feldspar, and elongated domains of phyllosilicates (Figure 7c and e). This foliation is at a low angle to the slip plane and is asymptotically curved towards it. In the foliated layer, the grain size is significantly reduced and the porosity is decreased, with respect to undeformed material. In certain cases, breccia zones are also present locally and are parallel to the high strain foliated layer along the slip planes (Figure 7c).

High pressure experiments (Griggs-type rig):

All the high-pressure experiments were carried out in shear geometry. Unlike the low-pressure experiments described above, the deformation is not localized along the sample-piston boundary, but along a fracture zone at a low angle to such boundary, with a synthetic sense of motion (Supplementary Material S4). Present along the fracture plane is a breccia layer, a few microns- to a at most a few tens of microns-thick and characterized by a large grain size reduction and a large porosity compared to the host rock.

Additionally, in three of the four samples (TM610BM, OR87BM, OR92BM), ductile deformation is also present within a foliated layer that can reach several hundreds of micrometers of thickness, located between the fracture/slip plane and the undeformed host rock. The foliation is defined by the preferential elongation of phyllosilicates, quartz/felspar and pyrite aggregates (Figure 8). Towards the slip plane, within the ductile deformation zone, a high strain layer is present locally, as is apparent by the deflection of the foliation towards the slip plane and a decrease in grain size (Figure 8).

3.2.3 Raman

One potential bias of deformation experiments is the actual temperature field. Heat conduction across the experimental samples potentially leads to temperature gradients across the sample between the lower and the upper alumina piston (Pec et al., 2016), and thus these gradients might influence the RSCM parameters. To assess this possibility, we determined whether any R1 variations were present and if they were systematic with respect to the distance to upper and lower alumina piston.

At low pressures (Paterson rig), sample PP649, which was deformed to bulk strain larger than 10% and without localization of the deformation, shows R1 values of 0.622+/-0.025 (standard deviation), i.e. minimal variations and no systematic trend with respect to the position within the sample. As a result, for Paterson deformation experiments, comparisons of R1 values across the whole sample can be performed.

Conversely, in high pressure experiments (TM609BM), measurements in similar, undeformed material near the upper and lower alumina pistons showed systematic R1 differences (0.804+/-0.082 for top vs. 1.013+/-0.075 for bottom), consistent with a temperature gradient across the sample (because of the heat conduction described above), and as a consequence R1 values could not be connected solely to strain. As a result, for Griggs-type experiments we focused only on carbonaceous particles across relatively small distances (of the order of a few hundreds of µm).

3.2.3.1 Breccia zones

Few measurements were carried out in breccia zones, because of the difficulty finding appropriate particles that could be analyzed according to the protocol. In the lower pressure sample PP633, a slight increase in R1 (~+5%) is observed compared to undeformed host rock in the two piston-sample boundaries, wherein fracturing is pervasive (Figure 9). In a higher-pressure sample, a fractured zone contains CM particles with a R1 ratio that is slightly higher, by 3% on average, than the undeformed host rock nearby (Figure 10). Given the many parameters, external to CM crystallinity, which may influence the Raman spectra, in particular the increase in sample fluorescence in fine-grained zones, it is highly questionable whether strain itself has an influence on CM crystalline organization.

3.2.3.2 Ductile strain zones

A significant increase in R1 is observed from undeformed zones to foliated, high strain domains next to the slip planes, irrespective of the low or high-pressure conditions (Figures 10 and 11, Supplementary Materials S5). In these three examples, the increase ranges from +4 to +41% (the values are defined as averages over microstructural domains). In samples where gradients of strain are visible as variations in the grain size and the preferred orientation of the microstructural elements, the increase in R1 is correlated with the increase in strain (Figures 10 to 12). The largest increase, +41%, is observed in the low-porosity high-strain zone of sample OR92BM (Figure 10). From all the possible parameters computed from RSCM spectra, R1 is the parameter that shows the most systematic and the largest variation as a function of strain (Figure S10).

3.2.4 Chemical changes in the high-strain zones

EDS compositional mapping was performed in zones with deformation gradients in low pressure sample PP641. Clasts in the undeformed domains are composed of quartz, albite and K-feldspar, whereas the matrix is composed of illite and chlorite (Figure 13). In the high-strain layer adjacent to the slip plane, the clasts are elongated and define a foliation bending towards the slip plane. These elongated clasts, originating from feldspar grains, contain both K and Na, i.e. have an intermediate composition between albite and K-feldspar. The distribution of these two elements is relatively heterogeneous. The BSE imaging of these chemically mixed zone revealed the comminution of the original feldspar, along with a very large microporosity.

4. Discussion

4.1 Kinetics of maturation in static heating experiments

4.1.1 Relevant Raman parameters to track crystallinity increase during heating

In both nature and experiments the increase in temperature affecting CM particles leads to an evolution in chemical and crystalline structure and is reflected in changes in the Raman spectrum (Beyssac et al., 2002; Lahfid et al., 2010; Li et al., 2006; Pasteris and Wopenka, 1991; Wopenka and Pasteris, 1993). Accordingly, a wealth of Raman parameters have been proposed as proxies of temperature, such as peak area ratios (Beyssac et al., 2002; Lahfid et al., 2010), peak width (Kouketsu et al., 2014), amplitude ratios of the peaks resulting from the raw spectrum deconvolution (Ito et al., 2017) or amplitude ratio of the maxima of the raw spectrum (Kaneki and Hirono, 2018, 2019; Kaneki et al., 2016).

In the static heating experiments shown here (Figure 3, figure S3 and Table 2), several parameters, such as D1 FWHM, RA1 and R2 area ratios, and R1 intensity ratio, evolve as a function of heating intensity and duration. Amongst these different parameters, the R1 intensity ratio (Figure 4) is the best proxy for CM crystallinity. Justifications for this conclusion are, first, the R1 is the parameter that shows monotonic variations, except for one experiment with HN78 (Figure S3), enabling the derivation of quantitative laws of evolution. Second, the correlation of R1 with temperature is demonstrated from earlier studies, both in natural metamorphic samples (Kouketsu et al., 2014; Lahfid et al., 2010) and in experimentally statically heated ones (Kaneki et al., 2016; Li et al., 2006; Muirhead, 2012). According to Li et al. (2006), the increase in R1 reflects the relative increase, upon heating, of the concentrations of aromatic rings having six or more fused benzene rings. Finally, in experiments of deformation, R1 intensity ratio is the most widely reported variable, enabling the effect of deformation on CM crystallinity to be studied (see Table 5 for the compilation of available studies). Please note that we have used the intensities defined as maxima on the full spectrum (Kaneki and Hirono, 2018, 2019; Kaneki et al., 2016) (Figure 4), and not as amplitude of the peaks obtained through peak fitting procedure (e.g., Ito et al. (2017)).

4.1.2 Kinetic model of Raman spectrum evolution upon heating

As discussed above, the R1 ratio evolution is monotonic in the range of experimental heating conditions considered. To derive the kinetic laws that link the R1 parameter to duration of heating and

temperature, we followed the method presented in Nakamura et al. (2017, 2020) for higher degrees of crystallinity (i.e., graphitization stage). Previous studies for simple evolution proposed the use of a power rate model or the Johnson-Mehl-Avrami (JMA) model (Huang, 1996; Muirhead, 2012); however, carbonization, similar to graphitization, is not a simple chemical reaction, but the result of simultaneous reactions (formation of basal structural units, devolatilization and crystal growth). Therefore, in order to model the complex chemical evolution of the CM, we preferred to use the method proposed by Nakamura et al. (2017), using a sigmoidal function with the following equation:

$$R1(T,t) = R1_{min} + \frac{(R1_{max} - R1_{min})}{1 + \left[\frac{t_{half}}{t}\right]^{h}} \quad (1)$$

where from the immature, original state ($R1_{min}$), a sharp evolution in R1 is observed (at high temperature) over few hours, after which R1 remains close to $R1_{max}$. In this equation, t_{half} and h are the inflection point and the order of reaction, called "Hill coefficient" of the sigmoid function, respectively. The parameter t_{half} could be described following an Arrhenius relation as:

$$t_{half} = A\,exp\left(\frac{-m}{T}\right) \quad (2)$$

Combining the equations (1) and (2), we obtained:

$$R1(T,t) = R1_{min} + \frac{(R1_{max} - R1_{min})}{1 + \left[\frac{A\,exp\left(\frac{-m}{T}\right)}{t}\right]^{h}} \quad (3)$$

Where $R1_{min}$ and $R1_{max}$ are the minimum and maximum R1 values, respectively; A is the intercept and m the slope of the Arrhenius plot; T and t are the temperature and the time of heating, respectively.

The full procedure is explained in Supplementary Materials S6. Results of the fitting procedure applied to static heating experiments are shown in Table 4 and Figure 14 for the two samples analyzed. The parameters for sample HN78 are close to the ones obtained in Moris-Muttoni et al. (2022), but are more reliable as they are calculated from a larger experimental dataset. Form Figure 14, one can also observe that the initial heating stage (at rates of 4.5°C/min) introduces negligible

errors, because before reaching high temperatures, such as 700°C or above, the evolution of R1 is very slow compared to the duration of heating.

Finally, these kinetic laws can be used in the deformation experiments described hereafter to predict the contribution of sole heating to the evolution in the crystalline organization of the CM.

4.2 Deformation processes

We analyze here first what types of deformation processes were operating in the experiments we performed, and which natural conditions of deformation these experiments are relevant for.

Two apparatuses were used, with contrasting conditions of confining pressure. At low pressure, the principal slip zone is localized along the sample-piston boundary, whereas at high pressure, strain is accommodated by a synthetic fracture zone cutting through the sample. In spite of these different geometries, the microstructures observed are relatively similar, as we systematically observed a breccia zone along the main slip interfaces. The breccia layers, defining the slip plane, are characterized by a large grain-size decrease with respect to starting material, clasts of variable size but with angular shapes and small aspect ratios, and a large porosity (Figures 7 and 8, Supplementary Material S4).

We also observed, along certain slip surfaces, high-strain foliated layers. These layers are characterized by small grain size, elongated and preferentially orientated grains or grain aggregates, and a reduced microscopic porosity (Figure 8). At smaller scale, in the elongated feldspar aggregates present in the high-strain layer, pervasive grain comminution, accompanied with a widespread submicron porosity, is visible (Figure 13).

Pec et al. (2016) analyzed the semi-brittle flow of granitoids in high pressure experiments, at lower temperature but higher strain rates, than the experiments described here. In their experiments, where the starting grains are two orders of magnitude larger than in ours, localized zones of deformation form, first Riedel shear zones then macroscopic shear-plane parallel ones. The sequence of processes starts with ductile deformation of the grains accompanied by pervasive grain fracturing, followed by the formation of an amorphous layer in the highest-strain zone. The pervasive grain fracturing in the

plagioclase in Pec et al. (2016) is accompanied by chemical exchanges and enrichment in K, which the authors interpret as reflecting the operation of dissolution-precipitation. The chemical patterns in plagioclase from the high strain zone reported here suggest that the same processes are active.

Deformation processes have therefore resulted in the formation of two types of microstructures, characterized by contrasting porosity. In some cases these microstructures are next to each other, irrespective of the pressure (Figure 7, low pressure, and Figure 8 bottom, high pressure), raising questions as their relative contribution to total strain, or their simultaneity. In the example of PP641, the relative contribution of the breccia and the high strain foliated layer is unraveled by the thin layer of pyrite connecting the two large fragments of the original grain on both side of the slip zone (Figure 7b). The thin layer of pyrite, parallelized to the slip plane, is within the high strain foliated zone, suggesting that most of the total strain is accommodated there, and not on the breccia layer next to it. Furthermore, in PP641 deformation experiments, as well as in all low-pressure, constant strain-rate experiments, the macroscopic stress-strain curve shows the alternation of two types of behavior, either stick-slip events or steady-state creep (Figure 5). Stick-slip events and creep accommodated a small and a large fraction of total strain, respectively. This comparison between the macroscopic behavior and the strain accommodated suggests that breccia formed during stick-slip events, whereas high strain foliated zones formed during creep. This interpretation is consistent with the microphysical models and the frictional viscous rheology (Den Hartog and Spiers, 2014; Niemeijer, 2018; Niemeijer et al., 2002), wherein the microstructures are interpreted to be the result of the competition between chemically-induced, dissolution-precipitation mediated, compaction and strain-induced porosity creation. In the highest strain-rate zone, on the slip plane itself, high porosity breccia forms because dissolution-precipitation is slower than strain-induced grain fracturing and dilatancy. In the layers next to the breccias, strain-rate is lower, dissolution-precipitation reactions in combination to grain-size reduction lead to rearranging the grains and closing up of the pores.

The case of high-pressure experiments is more problematic, as breccia and high strain foliated layers are both present (Figure 8), whereas no stick-slip events occurred. In the high-pressure experiments by Pec et al. (2016) reported above, or in Marti et al. (2017), porous breccia such as shown in Figure 8-

bottom are absent, while they observed zones of very high, ductile strain similar to the high strain foliated layers described in the present study. A peculiarity of the experiments carried out here, compared to Pec et al. (2016) or Marti et al. (2017), is the abundance of hydrous clays, such as smectite-illite, which may release water during the deformation at high temperature. Water release is a factor favorable to the formation of breccia, as attested by hydraulic fracturing structures observed in nature (e.g., Jebrak (1997)). Nonetheless, further experimental work is necessary to decipher the factors that control the types of microstructures that form during high-pressure deformation experiments.

In summary, the concomitant operation of brittle-fracturing and dissolution-precipitation operating in our experiments (Figure 13), similar to the observations in Pec et al. (2016), support the interpretation of semi-brittle deformation regime. This regime of deformation prevails in the seismogenic range of depths, i.e., the upper part of the crust where temperature conditions are lower than ~300-350°C (Sibson, 1977; Hyndman et al., 1997; Scholz, 1990). The high-strain foliated microstructures formed in the experiments of the present study mimick the ductile structures and microstructures of deformation present in the corresponding range of natural conditions (e.g., Raimbourg et al., 2019).

4.3 Effect of deformation on Raman signature and crystallinity of carbonaceous matter

4.3.1 Strain or shear heating?

Deformation, irrespective of its rate, releases some energy, hence raises locally the temperature. The amplitude of the local temperature rise needs to be evaluated, in order to discriminate the influence of deformation from the temperature onto the Raman signature of carbonaceous matter. In the deformation experiments we performed, order-of-magnitude calculations (Supplementary Material S7) show that the effect of temperature on the Raman signal is limited to low-pressure experiments, where stick-slip events occurred. Furthermore, this effect is restricted to a layer at most ~1µm-thick along the slip surface.

As a consequence, except for these very restricted zones, all the Raman signal variations observed in the present study can be safely connected to strain and not to temperature effect. In particular, the large increase in R1 observed in large-strain zones, within a layer of ~50 µm thick (Figure 11), cannot be attributed to transient heat pulses during stick-slip events and is therefore the result of strain. Semi-brittle, ductile deformation, similar to what can be observed in the "seismogenic" range of conditions in nature, has an undisputable and large effect on the increase in crystallinity of CM particles.

4.3.2 Interpretation of R1 increase in terms of crystallinity of carbonaceous particles

The static heating experiments reported in Section 4.1, similarly to other experimental studies (Deldicque et al., 2016; Hirono et al., 2015; Li et al., 2006), are consistent with an increase in R1 with increasing temperature. The deformation experiments reported in section 4.2 show that strain has a similar effect to temperature and tends to increase R1, in comparison to undeformed material.

All the Raman spectra analyzed in the present work are composed of five characteristic bands, typical of the low T conditions (up to ~330°C) that correspond to the carbonization stage (Lahfid et al., 2010). In this range of T conditions, increase in metamorphic grade results in an increase in the relative height of the D band (Rahl et al., 2005) which reflects an increased structural ordering of the carbonaceous matter. The increase in R1 observed in deformation zones (Figures 10 and 11) therefore reflects an increased crystallinity. Thus, strain has a catalytic effect on the process of carbon ordering.

For T above 330°C (the graphitization stage), on the contrary, increased metamorphism results in the decrease in the height and amplitude of the defect band (Beyssac et al., 2002; Kouketsu et al., 2014). This two-stage evolution, which led to define several Raman-based geothermometers depending on the T range considered (Beyssac et al., 2002; Lahfid et al., 2010), restricts the application of the present study to the relevant T range, namely the low range, where carbonization operates.

4.3.3 Comparison with other experimental studies

Many high-velocity experiments have tried to reproduce the evolution of CM crystallinity in fault zones as a result of seismic slip (Table 5). Invariably, these experiments have shown that at seismic slip velocities (~m/s), an increase in CM crystallinity in zones of highest slip is observed for low-grade

starting CM (Aubry et al., 2018; Bustin et al., 1995; Furuichi et al., 2015; Kaneki and Hirono, 2018, 2019; Oohashi et al., 2011; Savage et al., 2018). This conclusion does not hold for higher grade CM material evolving within the graphitization stage, as contrasting evolution, i.e., increase (Kuo et al., 2017) or decrease in crystallinity (Kaneki and Hirono, 2019; Kirilova et al., 2017), is observed. We therefore restrict the discussion here to the processes affecting low-grade CM material evolving within the carbonization stage, similar to the present study.

In all the high-velocity experiments cited above, a large temperature increase is predicted, and the evolution of CM towards higher crystallinity that is observed is interpreted as the result of this flash heating within the principal slip zone. Nonetheless, this effect of temperature does not exclude the possible complementary effect of strain.

Several friction studies have carried out tests at different slip velocity, encompassing seismic (~m/s) to subseismic (~100µm to 50mm/s) slip rates. These friction experiments are consistent with a large influence of the slip velocity, and the CM particle evolution at low slip rates is non visible (Oohashi et al., 2011). Note, that these friction experiments are carried out at ambient temperature and low (~1-10MPa) normal stress.

Slow strain rate experiments have also been carried out at high pressures and temperatures in a Griggs-type apparatuses, similar to the experiments of the present study (Bustin et al., 1995; Wilks et al., 1993). It has been shown in these experiments that strain promotes the reorientation, alignment and coalescence of the basal structural units made of polyaromatic layers, the reduction of the porosity, and overall an evolution of carbonaceous matter towards graphite structure. This evolution, supported by TEM and XRD anlayses, is recorded in the Raman signal by an increase in R1 ratio similar to the one observed in the present study. Bustin et al. (1995) note the discrepancy between the different evolution (TEM and XRD vs. Raman), where the latter show an apparent increase in the defect band, whereas the two other techniques show an increased organization of the crystalline structure. We remark here that this increase in R1 with increasing maturity, although its atomic-scale interpretation is unclear, is exactly the same as the one observed in natural rocks in the carbonization stage

(Kouketsu et al., 2014; Rahl et al., 2005), and was also observed experimentally as a result of heating (Li et al., 2006).

Slow strain-rate experiments therefore confirm the effect of strain on enhancing the crystallinity of low-grade CM, similar to the present study. Furthermore, the comparison of different experimental conditions highlights the major role of confining pressure and temperature: at room conditions, experiments are unable to reproduce the effect of strain, which is observable only under the conditions of high pressure and temperature that are relevant to natural shear and fault zones. Finally, a direct effect of pressure on enhancing CM maturation is also apparent from the comparison of Paterson and Griggs-type experiments (150MPa vs. 1 GPa of confining pressure) carried out at 600°C. In undeformed zones, at 1 GPa for 20hrs, (OR92BM), R1 reaches 0.69, while at 150 MPa for 42hrs (PP641) and 75hrs (PP649), R1 reaches only 0.62.

4.3.4 Comparison with natural studies

In naturally deformed samples, numerous studies have focused on the characteristic of CM particles in zones that concentrates deformation, in order to decipher the deformation processes. For low-grade CM material in the range of temperature corresponding to carbonization, most studies have recorded an increase in crystallinity in zones of strain, based on the RSCM signal (Ito et al., 2017; Kaneki et al., 2016), biomarkers (Savage and Polissar, 2019; Savage et al., 2014) or vitrinite reflectance (Suchy et al., 1997) (Table 5). These studies were, for the largest fraction of them, focused on fault zone material, hence they analyzed rocks that localized both strain and (potentially) heat production/temperature rise. While temperature was considered as the main factor causing the increase in the crystallinity of CM particles within fault zones (Ito et al., 2017; Kaneki et al., 2016; Savage and Polissar, 2019; Savage et al., 2014), the results of the present experimental study show that the Raman anomalies in fault zone rocks are ambiguous and difficult to interpret, as both temperature AND strain have an influence on CM crystallinity and the associated Raman signature. This complexity is illustrated in the datasets of natural fault zones ranging from low-grade up to greenschist-facies conditions studied by Muirhead et al. (2021), where the authors reported an inconsistent evolution with either a decrease or an increase in R1 between fault rock and undeformed host rock. Muirhead et

al. (2021) suggests that the effect of strain is a function of the pre-deformation crystallinity of the CM particles.

Natural slow strain-rate structures of deformation have focused much less attention and corresponding studies are much fewer. Nonetheless, the three studies reported in Table 5 have all concluded to an increased crystallinity of carbonaceous matter zones of localized ductile strain (Kedar et al. 2020, Petroccia et al., 2022; Suchy et al., 1997), over a large range of temperature conditions. The interpretation of this increased crystallinity is nevertheless controversial, as Petroccia et al. (2022) and Suchy et al. (1997) invoke shear heating rather than strain, to account for the anomaly in Raman signature. In Kedar et al. (2020), a zone of concentrated strain within the overturned limb of a fold was characterized by a decrease in R1, but also interpreted as a strain-related increase in maturity. The starting material in Kedar et al. (2020) has spectra whose shape is transitional between the carbonization and graphitization stages, hence the interpretation of R1 variations is not straightforward.

As a summary, if natural, slow strain-rate structures of deformation show a systematic increase in CM crystallinity, the anomaly in Raman signal in high strain-rate structures such as fault zones is still relatively unclear. Beside strain, strain-rate itself may have a variable effect on CM crystallinity and Raman signal. This is illustrated in higher grade material during the graphitization stage, where two contrasting trends are observed and are a function of the type of deformation processes. In ductile shear zones, where strain-rate is low, strain is accompanied by increased CM crystallinity (Petroccia et al., 2022), whereas in fault zones, with cataclasites, ultraclasites and pseudotachylites, cutting across high-grade rocks, a decrease in CM crystallinity was reported (Nakamura et al., 2015). In the former case, the strain energy of viscous deformation is interpreted as promoting graphitization and in the latter case, high-velocity deformation promoted amorphization and decrease in crystallinity. How this relates to the carbonization stage is not known, but it is possible that slow, aseismic deformation and very rapid, seismic deformation have different influence on CM evolution.

4.4 RSCM geothermometry applied to naturally deformed rocks

Beyond its application to geothermometry (Bellanger et al., 2015; Berger et al., 2020; Delchini et al., 2016; Girault et al., 2020; Raimbourg et al., 2014), RSCM has also been applied to deformation zones in order to decipher the past temperature field, particularly the occurrence of flash heating during earthquakes (Kouketsu et al., 2017; Savage and Polissar, 2019). The present study demonstrated the effect of strain, independently of temperature, to influence the RSCM signal in low grade CM particles typically present in fault cores cutting across sedimentary terranes. Even more, high-resolution R1 profiles across several natural fault zones showed that R1 is principally controlled by strain, and not temperature (Moris-Muttoni et al., 2022). For these reasons, using RSCM to reconstruct the past temperatures experienced within natural fault zones is questionable.

Similarly, the effect of deformation to enhance crystallinity is an obstacle to the use of RSCM as a geothermometer in naturally strained rocks. The influence of deformation is significant, as illustrated in Figures 10 and 11. Although many field examples provide ample exposures of undeformed rocks, the issue is still central for rocks that are pervasively deformed, such as tectonic mélanges. This is for instance the case in the Japanese Shimanto Belt, where several units of tectonic mélanges show an anomaly in the crystallinity of carbonaceous matter, as inferred from vitrinite reflectance data (Sakaguchi, 1999). A geological scenario with local thermal anomalies might well account for the higher CM crystallinity in tectonic mélange units, but the high localization of strain in these units, and its effect of on CM crystallinity, is an alternative explanation.

5 Conclusions

The static heating experiments carried out in this work have shown that the evolution of CM is best tracked by the Intensity Ratio Raman parameter R1. The increase in R1 upon heating, from a low-grade starting material, follows the same trend as the one observed in natural metamorphic series. It is therefore interpreted as reflecting an increase in the structural ordering, within the range of evolution corresponding to carbonization.

The ductile deformation zones obtained experimentally at low and high pressure are also characterized by a large increase in R1, reflecting a higher crystallinity than undeformed material. These results

point to the influence of strain, at slow strain-rate and without local temperature increase, to reorganize CM crystalline structure.

The influence of strain on CM crystallinity potentially undermines all the conclusions drawn so far in many studies from the literature on naturally faulted rocks, where the anomaly in Raman signature of CM (compared to undeformed host rock) has been interpreted as reflecting coseismic shear heating during past earthquakes. As both heating and strain drives carbonaceous matter towards higher structural ordering, then the evolution presented in Figure 1 may equally be the product of intense shear heating and large amounts of finite strain.

Finally, our experimental results highlight the importance of performing experiments at high P and T to mimick natural processes at depth. In this way the effect of strain only, which becomes significant at confining pressures of 150 MPa, is the highest in experiments at 1GPa and is not visible in friction experiments carried out at a few MPa of normal stresses, can be determined.

Acknowledgments This work was supported by Institut National des Sciences de l'Univers funding scheme SYSTER. The authors also acknowledge support from both LabEx VOLTAIRE (ANR-10-LABX-100-01) and EquipEx PLANEX (ANR-11-EQPX-0036) projects. We thank Frédéric Savoie, Esteban Le Moing and Rémy Planckaert for their help with the experiments. We are grateful to the Editor Samuel Angiboust, David K. Muirhead and two other reviewers, for providing very detailed and insightful comments on the manuscript that were essential to improve it.

Table captions

Table 1: Characterization of chemistry and degree of crystallinity of the carbonaceous material of the starting materials (18NOB01A – HN78).

Table 2: Summary of the RSCM parameters measured for all static heating experiments for the non-metamorphic (18NOB01A) and very-low grade (HN78) starting materials. SD stands for standard deviation. In the range 320-330°C, both geothermometers were extrapolated.

Table 3: Details of the deformation experiments, resulting microstructures and Raman characteristics.

Table 4: Parameters obtained from the fitting procedure of R1 evolution for static heating experiments on 18NOB01A and HN78. Time t is in minutes and temperature T is in °C.

Table 5: Summary of CM properties in natural and experimental deformation zones. Note the difference in the treatment of Raman spectra, in particular the ratio of Disordered (D band) to Graphite band (G band): R1 is calculated from the ratio of the intensities of the raw spectrum (see Figure 4), while ID1/ID2 stands for the ratio of the intensities of the functions D1 and D2 used to deconvolute the raw spectrum. Peak area ratio R2 is similarly defined in Beyssac et al. (2002) as the area ratio of the D band over G band, based on the 4-bands deconvolution adapted to the graphite-like, highly-ordered carbonaceous matter. For the poorly-ordered carbonaceous matter within the carbonization stage, the increase in crystallographic ordering is reflected in an increase in both intensity or area ratio of the D band over the G band. Contrarily, for the highly-ordered carbonaceous matter within the graphitization stage, the increase in crystallographic ordering is reflected in a decrease in both intensity or area ratio of the D band over the G band.

References

Ammar, M. R., and Rouzaud, J. N., 2012, How to obtain a reliable structural characterization of polished graphitized carbons by Raman microspectroscopy: J. Raman Spectrosc., v. 43, p. 207-211.

Aoya, M., Kouketsu, Y., Endo, S., Shimizu, H., Mizukami, T., Nakamura, D., and Wallis, S., 2010, Extending the applicability of the Raman carbonaceous-material geothermometer using data from contact metamorphic rocks: J. Metamorphic Geol., v. 28, p. 895-914.

Aubry, J., Passelègue, F., Deldicque, D., Girault, F., Marty, S., Lahfid, A., Bhat, H. S., Escartin, J., and Schubnel, A., 2018, Frictional heating processes and energy budget during laboratory earthquakes: Geophys. Res. Lett., v. 45, p. 12,274-212,282.

Barker, C. E., 1988, Geothermics of petroleum systems: implication of the stabilization of kerogen thermal maturation after a geologically brief heating duration at peak temperature: U.S. Geological Survey Bulletin, v. 1970, p. 26-29.

Barzoi, S. C., 2015, Shear stress in the graphitization of carbonaceous matter during the low-grade metamorphism from the northern Parang Mountains (South Carpathians) — Implications to graphite geothermometry: International Journal of Coal Geology, v. 146, p. 179-187.

Barzoi, S. C., and Guy, B., 2002, Role of metamorphic strain in the cristallinity of graphite: the example of the graphitic schists from the Lotru valley (Carpathians, Romania): C. R. Acad. Sc. Paris, v. 334, p. 89-95.

Beaudoin, A., Augier, R., Laurent, V., Jolivet, L., Lahfid, A., Bosse, V., Arbaret, L., Rabillard, A., and Menant, A., 2015, The Ikaria high-temperature Metamorphic Core Complex (Cyclades, Greece): Geometry, kinematics and thermal structure: J. Geodynamics, v. 92, p. 18-41.

Bellanger, M., Augier, R., Bellahsen, N., Jolivet, L., Monié, P., Baudin, F., and Beyssac, O., 2015, Shortening of the European Dauphinois margin (Oisans Massif,Western Alps): New insights from RSCM maximum temperature estimates and $^{40}Ar/^{39}Ar$ in situ dating: J. Geodynamics, v. 83, p. 37-64.

Beny-Bassez, C., and Rouzaud, J. N., 1985, Characterization of carbonaceous materials by correlated electron and optical microscopy and Raman microspectroscopy: Scanning Electron Microscopy, v. 1, p. 119-132.

Berger, A., Engi, M., Erne-Schmid, S., Glotzbach, C., Spiegel, C., de Goede, R., and Herwegh, M., 2020, The relation between peak metamorphic temperatures and subsequent cooling during continent–continent collision (western Central Alps, Switzerland): Swiss J. Geosci., v. 113, no. 4, p. 1-18.

Beyssac, O., Goffé, B., Chopin, C., and Rouzaud, J. N., 2002, Raman spectra of carbonaceous material in metasediments: a new geothermometer: J. Metamorph. Geol., v. 20, p. 859-871.

Bonijoly, M., Oberlin, M., and Oberlin, A., 1982, A possible mechanism for natural graphite formation: Int. J. Coal Geol., v. 1, p. 283-312.

Buseck, P. R., and Bo-Jun, H., 1985, Conversion of carbonaceous material to graphite during metamorphism: Geochimica et Cosmochimica Acta, v. 49, p. 2003-2016.

Bustin, R. M., Ross, J. V., and Rouzaud, J. N., 1995, Mechanisms of graphite formation from kerogen: experimental evidence: Int. J. Coal Geol., v. 28, p. 1-36.

Carslaw, H. S., and Jaeger, J. C., 1959, Conduction of heat in solids, Great-Britain, Oxford: Clarendon Press, 510 p.:

Cermak, V., and Rybach, L., 1982, Thermal properties: Thermal conductivity and specific heat of minerals and rocks, *in* Angeneister, G., ed., Landolt-Börnstein: Zahlenwerte und Funktionen aus Naturwissenschaften und Technik: Berlin, Springer Verlag, p. 305-343.

Clerc, C., Lahfid, A., Monié, P., Lagabrielle, Y., Chopin, C., Poujol, M., Boulvais, P., Ringenbach, J.-C., Masini, E., and de Saint Blanquat, M., 2015, High-temperature metamorphism during extreme thinning of the continental crust: a reappraisal of the North Pyrenean passive paleomargin: Solid Earth, v. 6, p. 643-668.

Delchini, S., Lahfid, A., Plunder, A., and Michard, A., 2016, Applicability of the RSCM geothermometry approach in a complex tectono-metamorphic context: The Jebilet massif case study (Variscan Belt, Morocco): Lithos, v. 256-257, p. 1-12.

Deldicque, D., Rouzaud, J. N., and Velde, B., 2016, A Raman e HRTEM study of the carbonization of wood: A new Raman-based paleothermometer dedicated to archaeometry: Carbon, v. 102, p. 319-329.

Den Hartog, S. A. M., and Spiers, C. J., 2014, A microphysical model for fault gouge friction applied to subduction megathrusts: J. Geophys. Res., v. 119, p. 1510-1529.

Furuichi, H., Ujiie, K., Kouketsu, Y., Saito, T., Tsutsumi, A., and Wallis, S., 2015, Vitrinite reflectance and Raman spectra of carbonaceous material asindicators of frictional heating on faults: Constraints from friction experiments: Earth Planet. Sci. Lett., v. 424, p. 191-200.

Girault, J.-B., Bellahsen, N., Boutoux, A., Rosenberg, C., Nanni, U., Verlaguet, A., and Beyssac, O., 2020, The 3-D Thermal Structure of the Helvetic Nappes of the European Alps: Implications for Collisional Processes: Tectonics, v. 39, p. 1-20.

Henry, D. G., Jarvis, I., Gillmore, G., Stephenson, M., and Emmings, J. F., 2018, Assessing low-maturity organic matter in shales using Raman spectroscopy: Effects of sample preparation and operating procedure: Int. J. Coal Geol., v. 191, p. 135-151.

Hirono, T., Maekawa, Y., and Yabuta, H., 2015, Investigation of the records of earthquake slip in carbonaceous materials from the Taiwan Chelungpu fault by means of infrared and Raman spectroscopies: G-cubed, v. 16, p. 1233-1253.

Huang, W.-L., 1996, Experimental study of vitrinite maturation: effects of temperature, time, pressure, water, and hydrogen index: Organic Geochemistry, v. 24, p. 233-241.

Hyndman, R. D., Yamano, M., and Oleskevich, D. A., 1997, The seismogenic zone of subduction thrust faults: The Island Arc, v. 6, p. 244-260.

Ito, K., Ujiie, K., and Kagi, H., 2017, Detection of increased heating and estimation of coseismic shear stress from Raman spectra of carbonaceous material in pseudotachylytes: Geophys. Res. Lett., v. 44, p. 1749-1757.

Jebrak, M., 1997, Hydrothermal breccias in vein-type ore deposits: A review of mechanisms, morphology and size distribution. Ore Geology Reviews 12, p. 111-134.

Kaneki, S., and Hirono, T., 2018, Kinetic effect of heating rate on the thermal maturity of carbonaceous material as an indicator of frictional heat during earthquakes: Earth Planets Space, v. 70, no. 92, p. 1-10.

-, 2019, Diagenetic and shear-induced transitions of frictional strength of carbon-bearing faults and their implications for earthquake rupture dynamics in subduction zones: Scientific Reports, v. 9, p. 7884-7892.

Kaneki, S., Hirono, T., Mukoyoshi, H., Sampei, Y., and Ikehara, M., 2016, Organochemical characteristics of carbonaceous materials as indicators of heat recorded on an ancient plate-subduction fault: G-cubed, v. 17, p. 2855-2868.

Katagiri, G., Ishida, H., and Ishitani, A., 1988, Raman spectra of graphite edge planes: Carbon, v. 26, p. 565-571.

Kedar, L., Bond, C. E., and Muirhead, D. K., 2020, Carbon ordering in an aseismic shear zone: Implications for Raman geothermometry and strain tracking: Earth Planet. Sci. Lett., v. 549, p. 116536.

Kirilova, M., Toy, V., Rooney, J. S., Giorgetti, C., Gordon, K. C., Collettini, C., and Takeshita, T., 2017, Structural disorder of graphite and implications for graphite thermometry: Solid Earth, v. 9, p. 223-231.

Kohlstedt, D. L., Evans, B., and Mackwell, S. J., 1995, Strength of the lithosphere: constraints imposed by laboratory experiments: J. Geophys. Res., v. 100, no. B9, p. 17,587-517,602.

Kouketsu, Y., Mizukami, T., Mori, H., Endo, S., Aoya, M., Hara, H., Nakamura, D., and Wallis, S., 2014, A new approach to develop the Raman carbonaceous material geothermometer for low-grade metamorphism using peak width: Island Arc, v. 23, p. 33-50.

Kouketsu, Y., Shimizu, I., Wang, Y., Yao, L., Ma, S., and Shimamoto, T., 2017, Raman spectra of carbonaceous materials in a fault zone in the Longmenshan thrust belt, China; comparisons with those of sedimentary and metamorphic rocks: Tectonophysics, v. 699, p. 129-145.

Kuo, L.-W., Di Felice, F., Spagnuolo, E., Di Toro, G., Song, S.-R., Aretusini, S., Li, H., Suppe, J., Si, J., and Wen, C.-Y., 2017, Fault gouge graphitization as evidence of past seismic slip: Geology, v. 45, no. 11, p. 979-982.

Lahfid, A., Beyssac, O., Deville, E., Negro, F., Chopin, C., and Goffé, B., 2010, Evolution of the Raman spectrum of carbonaceous material in low-grade metasediments of the Glarus Alps (Switzerland): Terra Nova, v. 22, p. 354-360.

Lanari, P., Guillot, S., Schwartz, S., Vidal, O., Tricart, P., Riel, N., and Beyssac, O., 2012, Diachronous evolution of the alpine continental subduction wedge: Evidence from P–T estimates in the Briançonnais Zone houillère (France – Western Alps): J. Geodynamics, v. 56-57, p. 39-54.

Li, X., Hayashi, J.-I., and Li, C.-Z., 2006, FT-Raman spectroscopic study of the evolution of char structure during the pyrolysis of a Victorian brown coal: Fuel, v. 85, p. 1700-1707.

Marti, S., Stünitz, H., Heilbronner, R., Plümper, O., and Drury, M. R., 2017, Experimental investigation of the brittle-viscous transition in mafic rocks – Interplay between fracturing, reaction, and viscous deformation: J. Struct. Geol., v. 105, p. 62-79.

Marti, S., Stünitz, H., Heilbronner, R., Plümper, O., and Kilian, R., 2018, Syn-kinematic hydration reactions, grain size reduction, and dissolution-precipitation creep in experimentally deformed plagioclase-pyroxene mixtures: Solid Earth, v. 9, p. 985-1009.

Meneghini, F., Di Toro, G., Rowe, C.D., Moore, J.C., Tsutsumi, A. and Yamaguchi, A. (2010) Record of mega-earthquakes in subduction thrusts: The black fault rocks of Pasagshak Point (Kodiak Island, Alaska). GSA Bull. 122, 1280-1297.

Moris-Muttoni, B., Raimbourg, H., Augier, R., Champallier, R., and Le Trong, E., 2022, The impact of melt versus mechanical wear on the formation of pseudotachylyte veins in accretionary complexes: Scientific Reports, v. 12, no. 1529, p. 1-12.

Muirhead, D. K., 2012, A kinetic model for the thermal evolution of sedimentary and meteoritic organic carbon using Raman spectroscopy: Journal of analytical and applied pyrolysis, v. 96, p. 153-161.

Muirhead, D. K., Kedar, L., Schito, A., Corrado, S., Bond, C. E., and Romano, C., 2021, Raman Spectral Shifts in Naturally Faulted Rocks: G-cubed, v. 22, p. e2021GC009923.

Murata, A., 1997, Geological map of Miyazaki prefecture, 1:200,000: Miyazaki Prefectural Government.

Nakamura, Y., Oohashi, K., Toyoshima, T., Satish-Kumar, M., and Akai, J., 2015, Strain-induced amorphization of graphite in fault zones of the Hidaka metamorphic belt, Hokkaido, Japan: J. Struct. Geol., v. 72, p. 142-161.

Nakamura, Y., Yoshino, T., and Satish-Kumar, M., 2017, An experimental kinetic study on the structural evolution of natural carbonaceous material to graphite: American Mineralogist, v. 102, p. 135-148.

-, 2020, Pressure dependence of graphitization: implications for rapid recrystallization of carbonaceous material in a subduction zone: Contrib. Mineral. Petrol., v. 175:32, p. 1-14.

Niemeijer, A. R., 2018, Velocity-dependent slip weakening by the combined operation of pressure solution and foliation development: Scientific Reports, v. 8, p. 1-10.

Niemeijer, A. R., Spiers, C. J., and Bos, B., 2002, Compaction creep of quartz sand at 400-600°C: experimental evidence for dissolution-controlled pressure solution: Earth Planet. Sci. Lett., v. 195, p. 261-275.

Oberlin, A., 1984, Carbonization and graphitization: Carbon, v. 22, p. 521-541.

Oohashi, K., Hirose, T., and Shimamoto, T., 2011, Shear-induced graphitization of carbonaceous materials during seismic fault motion: Experiments and possible implications for fault mechanics: J. Struct. Geol., v. 33, p. 1122-1134.

Passelègue, F., Schubnel, A., Nielsen, S., Bhat, H., and Deldicque, D., 2016, Dynamic rupture processes inferred from laboratory microearthquakes: J. Geophys. Res.-Sol. Ea., v. 121, no. 6, p. 4343-4365.

Pasteris, J. D., 1989, In Situ Analysis in Geological Thin-Sections by Laser Raman Microprobe Spectroscopy: A Cautionary Note: Applied Spectroscopy, v. 43, p. 567-570.

Pasteris, J. D., and Wopenka, B., 1991, Raman spectra of graphite as indicators of degree of metamorphism: Canadian Mineralogist, v. 29, p. 1-9.

Paterson, M. S., 1990, Rock deformation experimentation, *in* Duba, A. G., Durham, W. B., Handin, W., and Wang, K. F., eds., The brittle-ductile tranition in rocks: Washington, D.C., American Geophysical Union, p. 187-194.

Pec, M., Stünitz, H., and Heilbronner, R., 2012, Semi-brittle deformation of granitoid gouges in shear experiments at elevated pressures and temperatures: J. Struct. Geol., v. 38, p. 200-221.

Pec, M., Stünitz, H., Heilbrönner, R., and Drury, M. R., 2016, Semi-brittle flow of granitoid fault rocks in experiments at mid-crustal conditions: J. Geophys. Res, v. 121, p. 1677-1705.

Petroccia, A., Carosi, R., Montomoli, C., Iaccarino, S., and Vitale-Brovarone, A., 2022, Deformation and temperature variation along thrust-sense shear zones in the hinterland-foreland transition zone of collisional settings: A case study from the Barbagia Thrust (Sardinia, Italy): J. Struct. Geol., v. 161, p. 104640.

Polissar, P.J., Savage, H.M., Brodsky, E.E., 2011, Extractable organic material in fault zones as a tool to investigate frictional stress: Earth Planet. Sci. Lett., v. 311, p. 439-447.

Précigout, J., Stünitz, H., Pinquier, Y., Champallier, R., and Schubnel, A., 2018, High-pressure, High-temperature Deformation Experiment Using the New Generation Griggs-type Apparatus: J. Vis. Exp., v. 134, p. e56841.

Rahl, J. M., Anderson, K. M., Brandon, M. T., and Fassoulas, C., 2005, Raman spectroscopic carbonaceous material thermometry of low-grade metamorphic rocks: Calibration and application to tectonic exhumation in Crete, Greece: Earth Planet. Sci. Lett., v. 240, p. 339-354.

Raimbourg, H., Augier, R., Famin, V., Gadenne, L., Palazzin, G., Yamaguchi, A., and Kimura, G., 2014, Long-term evolution of an accretionary prism: the case study of the Shimanto Belt, Kyushu, Japan: Tectonics, v. 33, p. 1-24.

Raimbourg, H., Famin, V., Palazzin, G., Sakaguchi, A., Yamaguchi, A., and Augier, R., 2017, Tertiary evolution of the Shimanto Belt (Japan): a large-scale collision in Early Miocene: Tectonics, v. 36, p. 1-21.

Raimbourg, H., Thiéry, R., Vacelet, M., Famin, V., Ramboz, C., Boussafir, M., Disnar, J.-R. and Yamaguchi, A.,2017, Organic matter cracking: a source of fluid overpressure in subducting sediments: Tectonophysics, v. 721, 254-274.

Raimbourg, H., Famin, V., Palazzin, G., Yamaguchi, A., Augier, R., Kimamura, Y., and Sakaguchi, A., 2019, Distributed deformation along the subduction plate interface: The role of tectonic mélanges: Lithos, v. 334-335, p. 69-87.

Rajic, K., Raimbourg, H., Famin, V., Moris-Muttoni, B., Fisher, D.M., Morell, K. and Canizares, A., 2023, Exhuming an Accretionary Prism: A Case Study of the Kodiak Accretionary Complex, Alaska, USA: Tectonics, v. 42, p. 1-25.

Ross, J.V., Bustin, R.M., 1990, The role of strain energy in creep graphitization of anthracite: Nature, v. 343, p. 58-60.

Ross, J.V., Bustin, R.M., Rouzaud, J.N., 1992, Graphitization of high-rank coals - the role of shear strain: experimental considerations: Organic Geochemistry, v. 17, p. 585-596.

Sadezky, A., Muckenhuber, H., Grothe, H., Niessner, R., and Pöschl, U., 2005, Raman microspectroscopy of soot and related carbonaceous materials: Spectral analysis and structural information: Carbon, v. 43, p. 1731-1742.

Sakaguchi, A., 1999, Thermal structure and paleo-heat flow in the Shimanto accretionary prism, Southwest Japan: The Island Arc, v. 8, p. 359-372.

Savage, H. M., and Polissar, P. J., 2019, Biomarker Thermal Maturity Reveals Localized Temperature Rise From Paleoseismic Slip Along the Punchbowl Fault, CA, USA: G-cubed, v. 20, p. 3201-3215.

Savage, H. M., Polissar, P. J., Sheppard, R., Rowe, C. D., and Brodsky, E. E., 2014, Biomarkers heat up during earthquakes: New evidence of seismic slip in the rock record: Geology, v. 42, no. 2, p. 99-102.

Savage, H. M., Rabinowitz, H. S., Spagnuolo, E., Aretusini, S., Polissar, P. J., and Di Toro, G., 2018, Biomarker thermal maturity experiments at earthquake slip rates: Earth Planet. Sci. Lett., v. 502, p. 253-261.

Sibson, R.H. (1977) Fault rocks and fault mechanics. Journal of the Geological Society, London 133, 191-213.

Scholz, C., 1990, The mechanics of earthquakes and faulting, Cambridge University Press, 439 p.:

Shuto, T., 1961, Palaeontological Study of the Miyazaki Group : A General Account of Faunas: Memoirs of the Faculty of Science, Kyushu University. Series D, v. 10, no. 73-206.

Suchy, V., Frey, M., and Wolf, M., 1997, Vitrinite reflectance and shear-induced graphitization in orogenic belts: A case study from the Kandersteg area, Helvetic Alps, Switzerland: Int. J. Coal Geol., v. 34, p. 1-20.

Tuinstra, F., and Koenig, J. L., 1970, Raman Spectrum of Graphite: The Journal of chemical physics, v. 53, p. 1126-1130.

Ujiie, K., Ito, K., Nagate, A., and Tabata, H., 2021, Frictional melting and thermal fracturing recorded in pelagic sedimentary rocks of the Jurassic accretionary complex, central Japan: Earth and Planetary Science Letters, v. 554, p. 116638.

Ujiie, K. and Kimura, G. (2014) Earthquake faulting in subduction zones: insights from fault rocks in accretionary prisms. Progress in Earth and Planetary Science 1, 1-30.

Wada, H., Tomita, T., Matsuura, K., Iuchi, K., Ito, M., and Morikiyo, T., 1994, Graphitization of carbonaceous matter during metamorphism with references to carbonate and pelitic rocks of contact and regional metamorphisms, Japan: Contrib. Mineral. Petrol., v. 118, p. 217-228.

Wang, Y., Alsmeyer, D.C. and McCreery, R.L., 1990, Raman spectroscopy of carbon material: structural basis of observed spectra. Chem. Mater. 2, 557-563.

Wilks, K. R., Mastalerz, M., Ross, J. V., and Bustin, R. M., 1993, The effect og experimental deformation on the graphitization of Pennsylvania anthracite: Int. J. Coal Geol., v. 24, p. 347-369.

Wopenka, B., and Pasteris, J. D., 1993, Structural characterization of kerogens to granulite-facies graphite: Applicability of Raman microprobe spectroscopy: American Mineralogist, v. 78, p. 533-557.

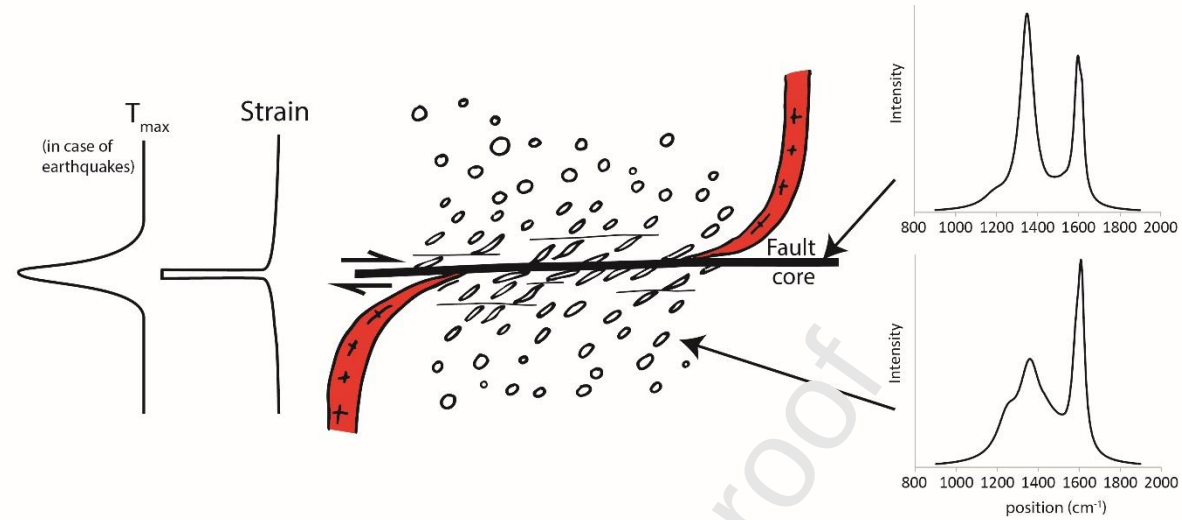

Figure 1 : Raman spectra of carbonaceous particles show anomalies, corresponding to higher crystallinity, in the core of fault zones (for example Moris-Muttoni et al., 2022). We are considering here conditions of deformation and metamorphism pertaining to the brittle field, up to brittle-ductile transition, hence regional temperatures in the range 150-350°C approximately. As illustrated on the left plots, fault cores are zones of both high strain and possibly high Tmax, i.e. maximum experienced temperature (if the fault slipped during earthquakes). While the role of temperature on Raman is, at least qualitatively, well established, the role of strain is not known, and constitutes the object of the present study.

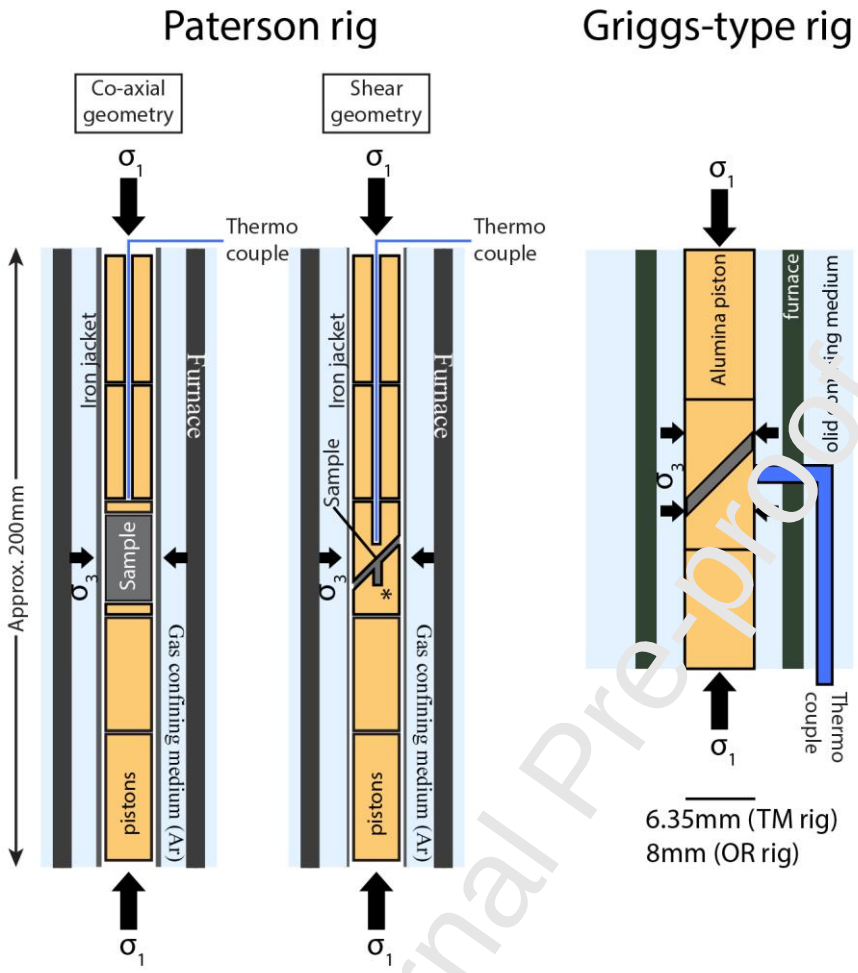

Figure 2 : Deformation experiment setup in the Paterson and Griggs-type rigs, with gas and solid confining media, respectively. In shear geometry with the Paterson rig, a cylinder of sample material (shown as *) is added to the 45°-cut sample to serve as an undeformed reference.

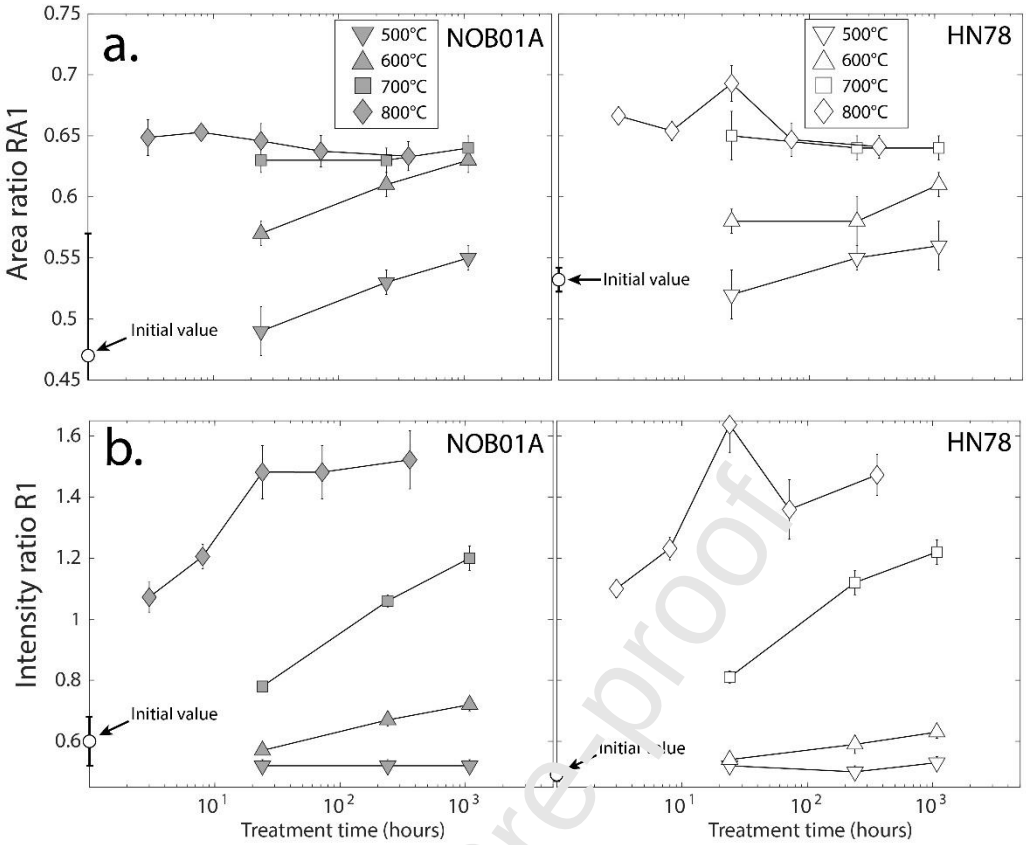

Figure *3* : Evolution of the RSCM parameters through the carbonization stage for 18NOB01A and HN78. **a.** RA1 area ratio (Lahfid et al., 2010). **b.** Intensity Ratio R1. The error bar is the standard deviation associated with the 20 CM particles/spectra analyzed on each experimental sample.

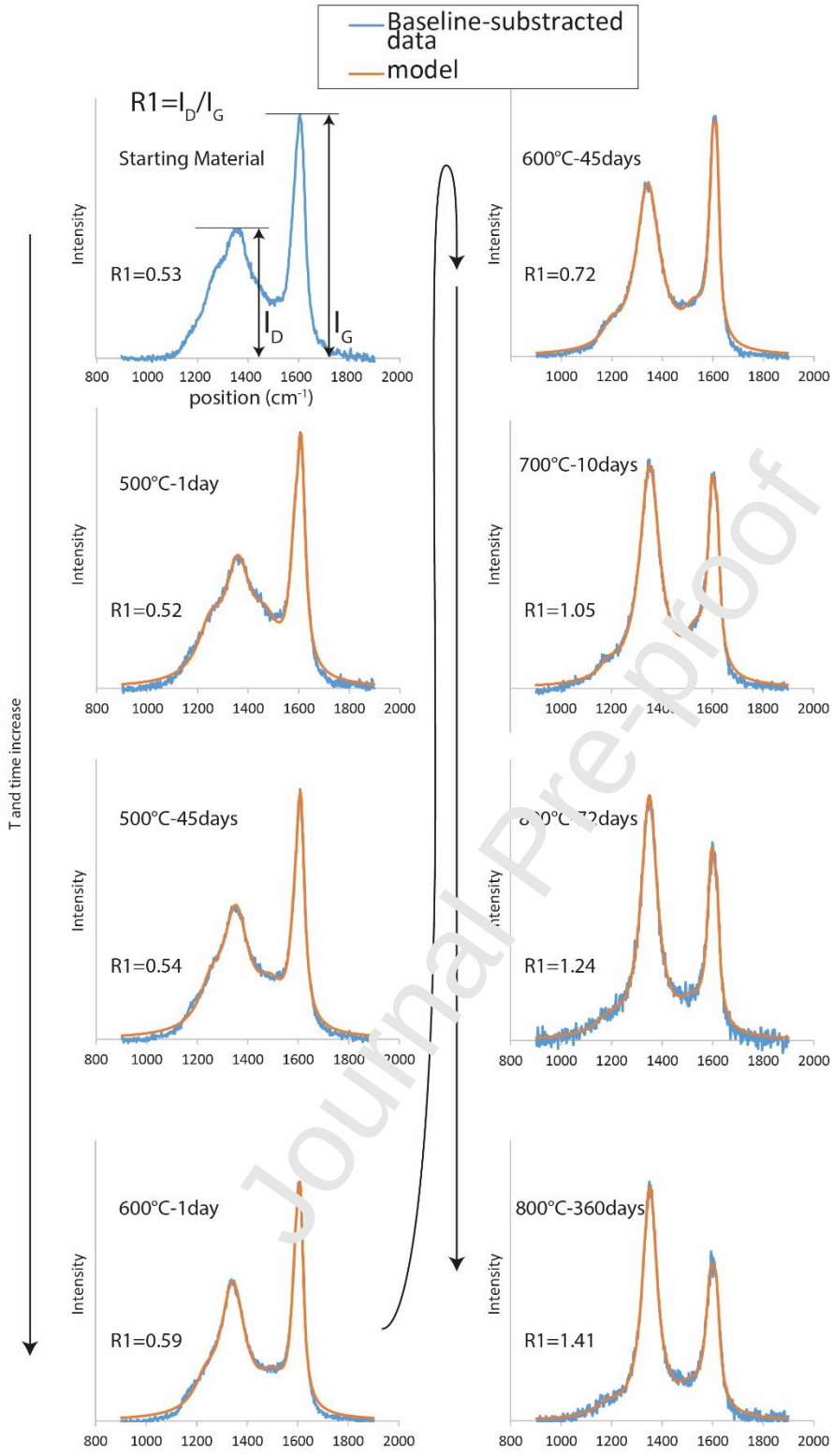

Figure *4*: Representative spectra (baseline-substracted and modelled as a result of peak-fitting procedure) showing the evolution with increased duration and temperature of static heating, for sample 18NOB01A. Intensities of the peaks vary between ~1000 and ~5500 counts between the different samples.

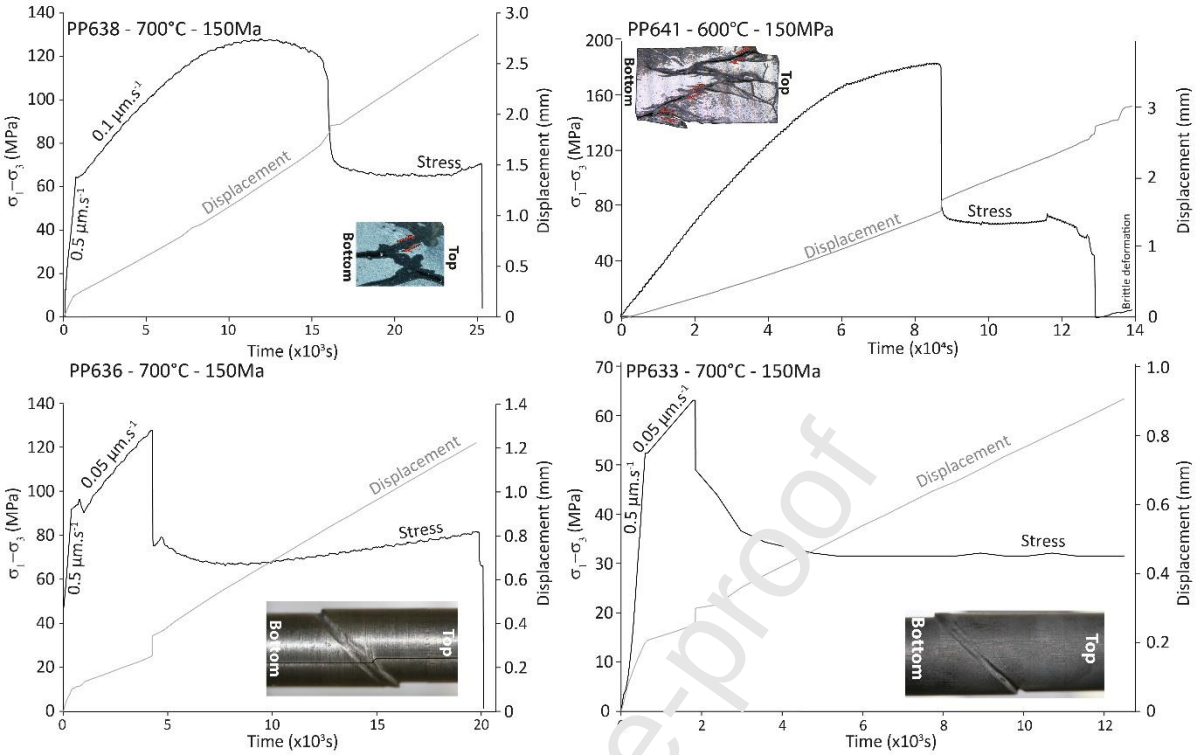

Figure 5 : Paterson rig experiments. Differential stress σ_1 - σ_3 and axial displacement curves as a function of time for coaxial (PP638 and PP641) and shear (PP633 and PP636) deformation experiments. Deformed samples photographs correspond to axial sections for PP638 and PP641 and to the external jacket for PP633 and PP636. In all photographs σ_1 is horizontal and σ_3 vertical.

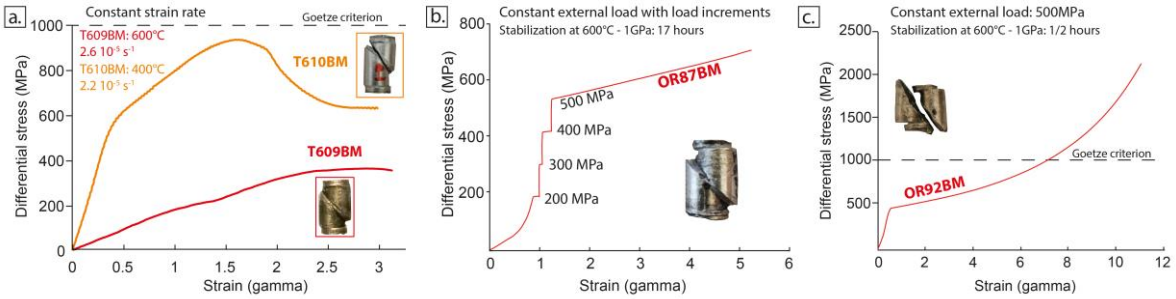

Figure 6 : Griggs-type rig experiments. (a) Constant strain rate experiments, at 400 and 600°C, (b) and (c), constant load experiments at 600°C. In (b), the sample was left for 17 hours at 600°C-1GPa before external loading with incremental steps from 100 to 500MPa. In (c), the sample was left for 1/2 hour at 600°C-1GPa before external loading at 500MPa. All experiments at 1GPa confining pressure. In constant load experiments, the actual differential stress on the sample is recalculated a posteriori as the stressed surface varies as a function of strain.

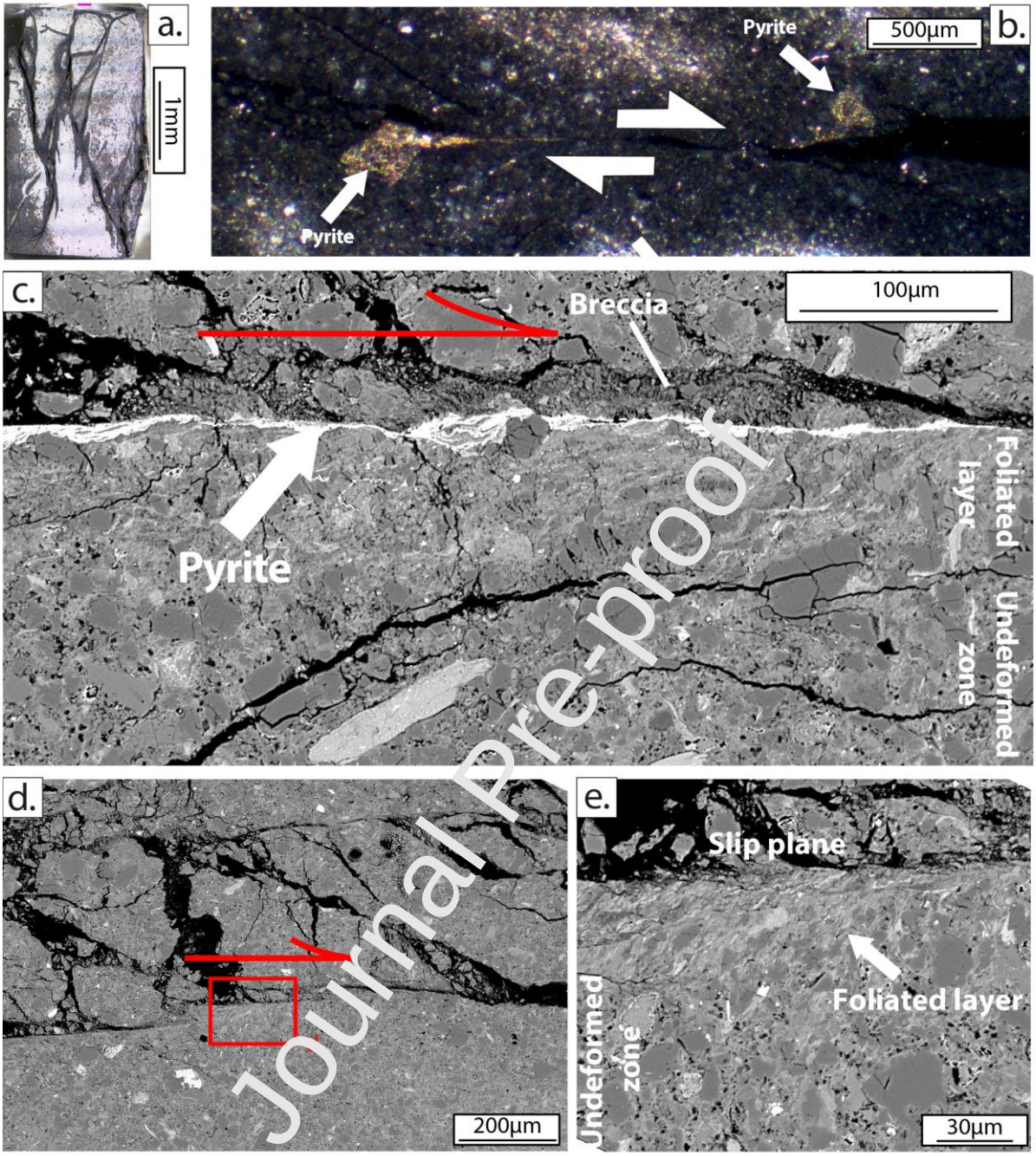

Figure 7 : Deformation microstructures observed for the Paterson Rig experimental sample PP641 deformed in coaxial geometry. **a:** cross-section of the whole sample, showing the conjugate fracture planes. **b**. Offset of a pyrite grain by a slip plane. **c-d-e:** The slip zone is bordered by a foliated layer, less than 50m-thick. In c, the slip zone is underlined by a bright layer of pyrite originating from the large pyrite grain and one side of the slip plane is composed of a breccia, the other one of a foliated zone. Note in c and e the decrease in porosity in the foliated zone compared to undeformed host-rock or to breccia. e is a close-up view of d. a: photograph, b: optical microscopy in reflected light, c to e: SEM-BSE imaging.

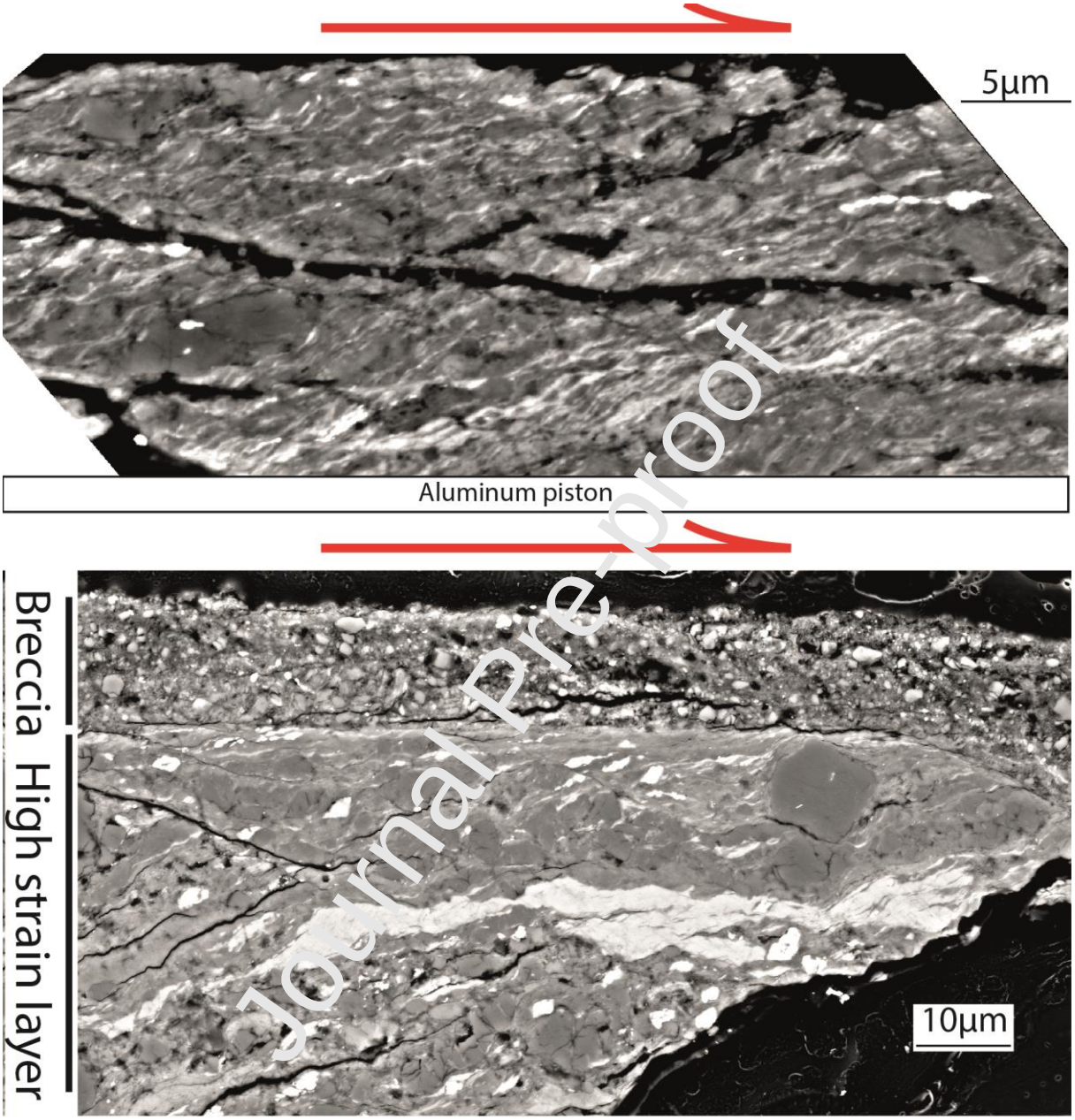

Figure 8 : High-strain layers in the vicinity of the main slip planes (shown by red arrows), in OR92BM (top) and TM610BM (bottom). These layers contain plyllosilicates defining a foliation at low-angle to the main slip plane. The grain size is of the order of the micron or lower, and the porosity is strongly reduced. Note in the bottom picture the juxtaposition of the high strain layer with a thin layer of breccia showing submicron-sized clasts and a much larger porosity. All images from SEM-BSE imaging.

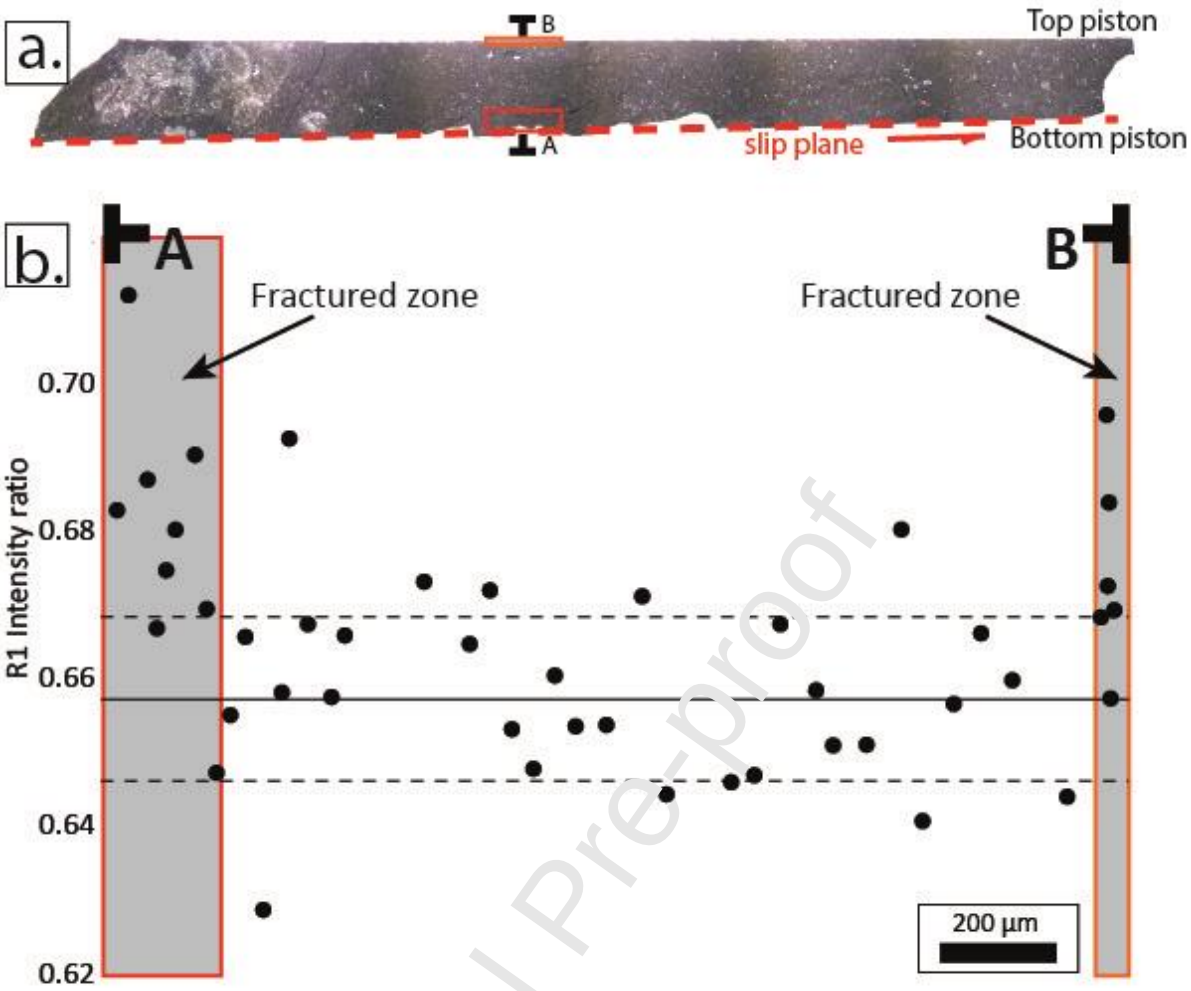

Figure 9 : RSCM results obtained for the sample PP633. **a.** Optical microscopy image in reflected light of sample PP633 showing the location of the RSCM profile and the two deformed zones. Slip was localized on the lower piston-sample boundary (dashed red line). **b.** Intensity ratio profile across the sample.

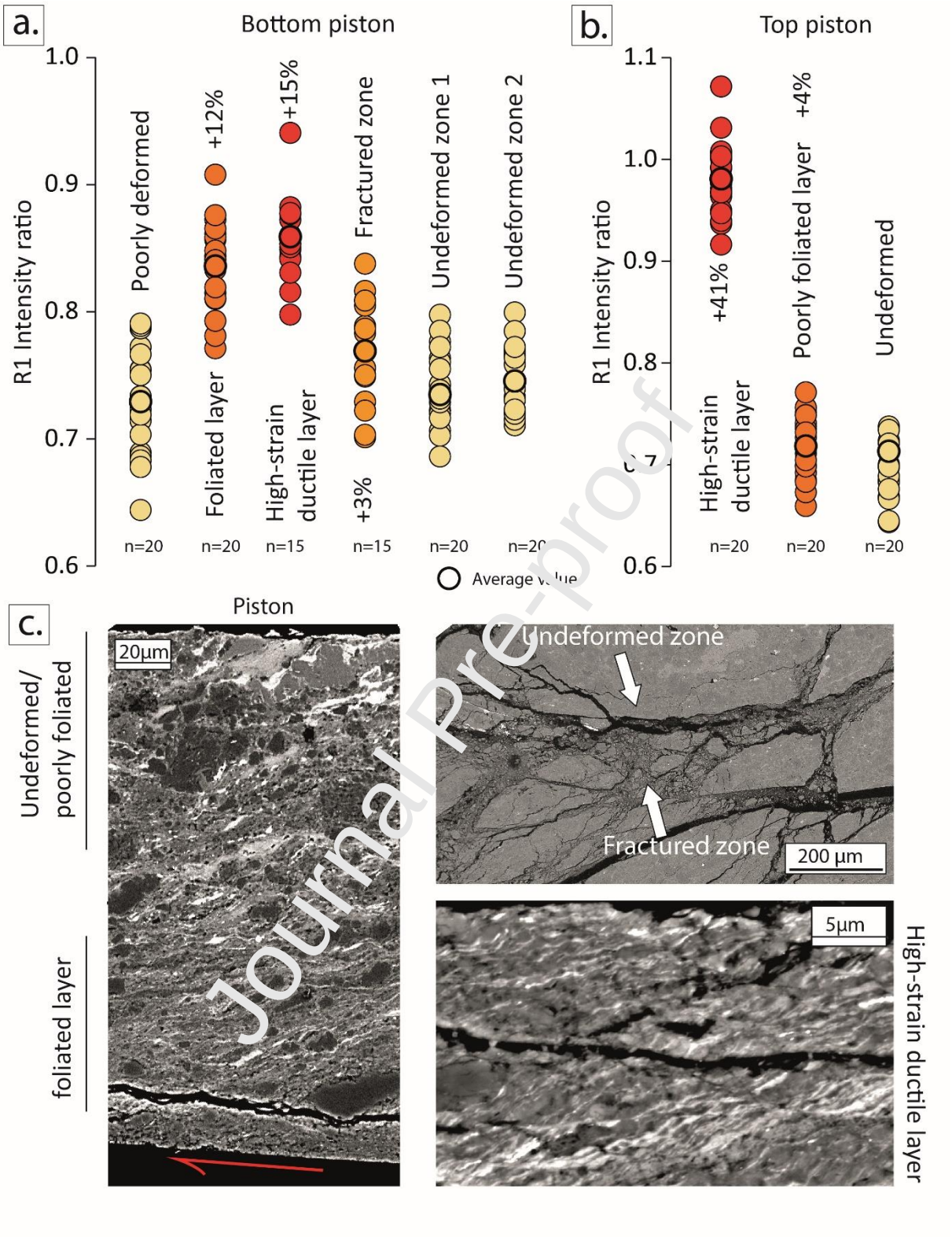

Figure 10 : RSCM results obtained for the sample OR92BM. **a. and b.** Diagram representing the R1 evolution in the different microstructural zones defined. A systematic increase in R1 is observed as a function of strain (the domains analyzed are in the vicinity of bottom piston (a) or top piston (b)) **c.** BSE imaging of the different microstructures.

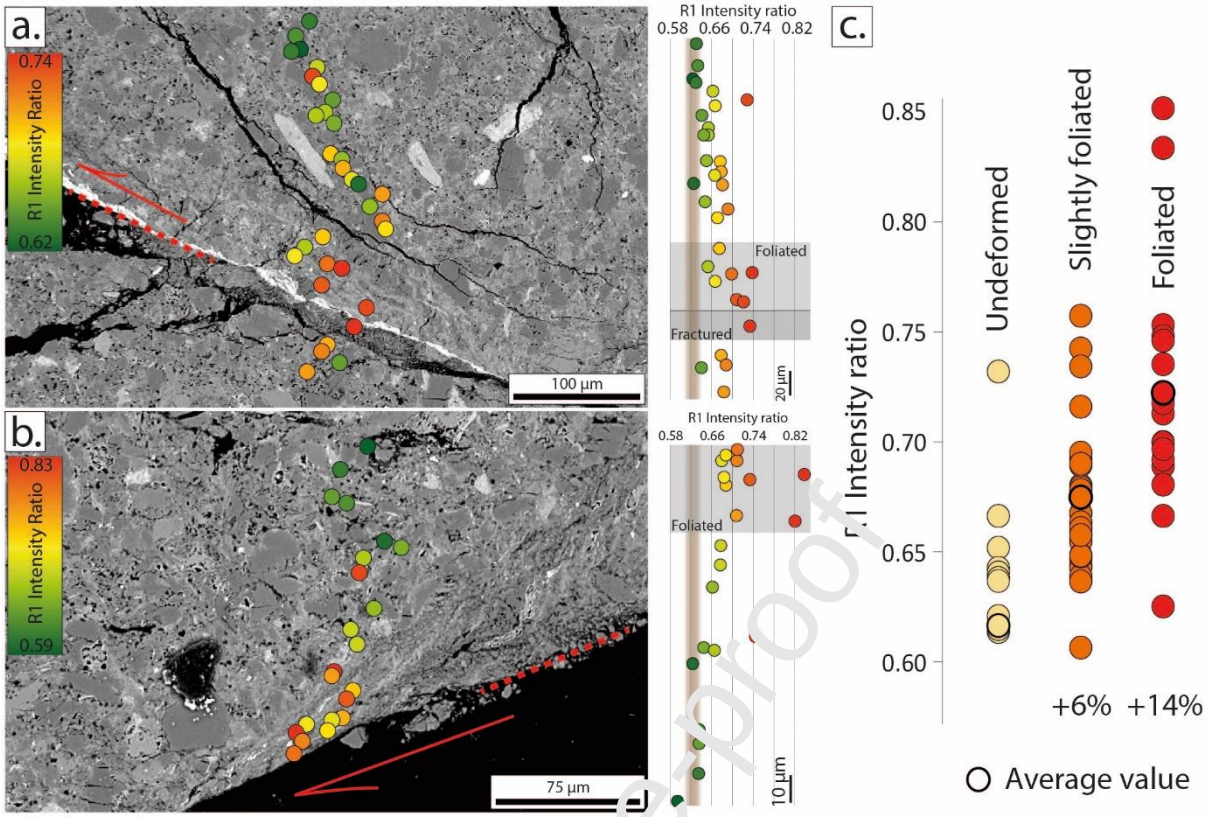

Figure 11 : RSCM results obtained for the sample PP641. **a. and b**. high-resolution R1 profiles obtained along the strained zones developed during the experiment. The slip surfaces are shown by a dashed red line, and the sense of shear is indicated by the arrows. **c.** R1 diagram by zones showing the evolution of the R1 in the undeformed, slightly foliated and foliated zones.

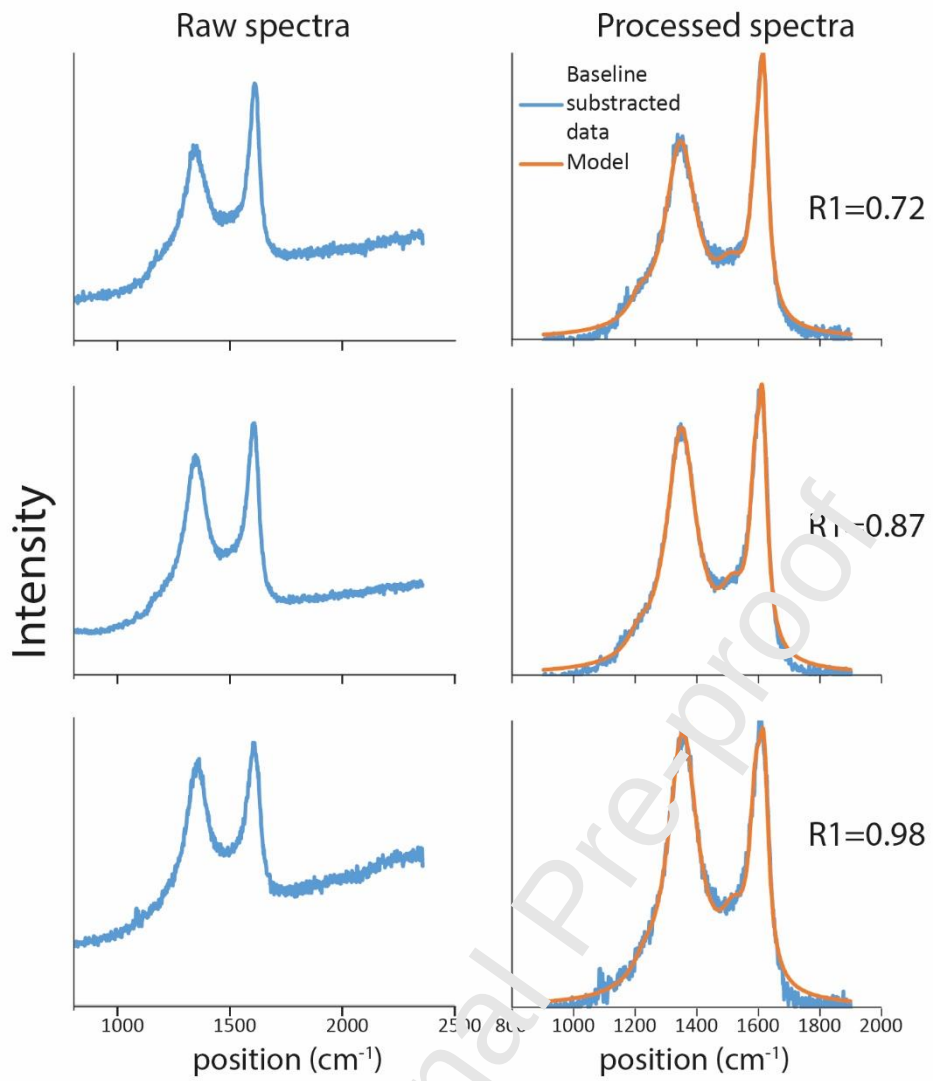

Figure 12: Representative RSCM spectra obtained for the sample OR92BM. Left: raw spectra; Right: Baseline-substracted spectra and their modelling as a result of peak-fitting procedure. R1 calculated on the modelled spectra shows large variations as a function of strain (Figure 10). The CM particles analyzed are located through a section across an undeformed (top), foliated (middle) and intensely foliated (bottom) zones.

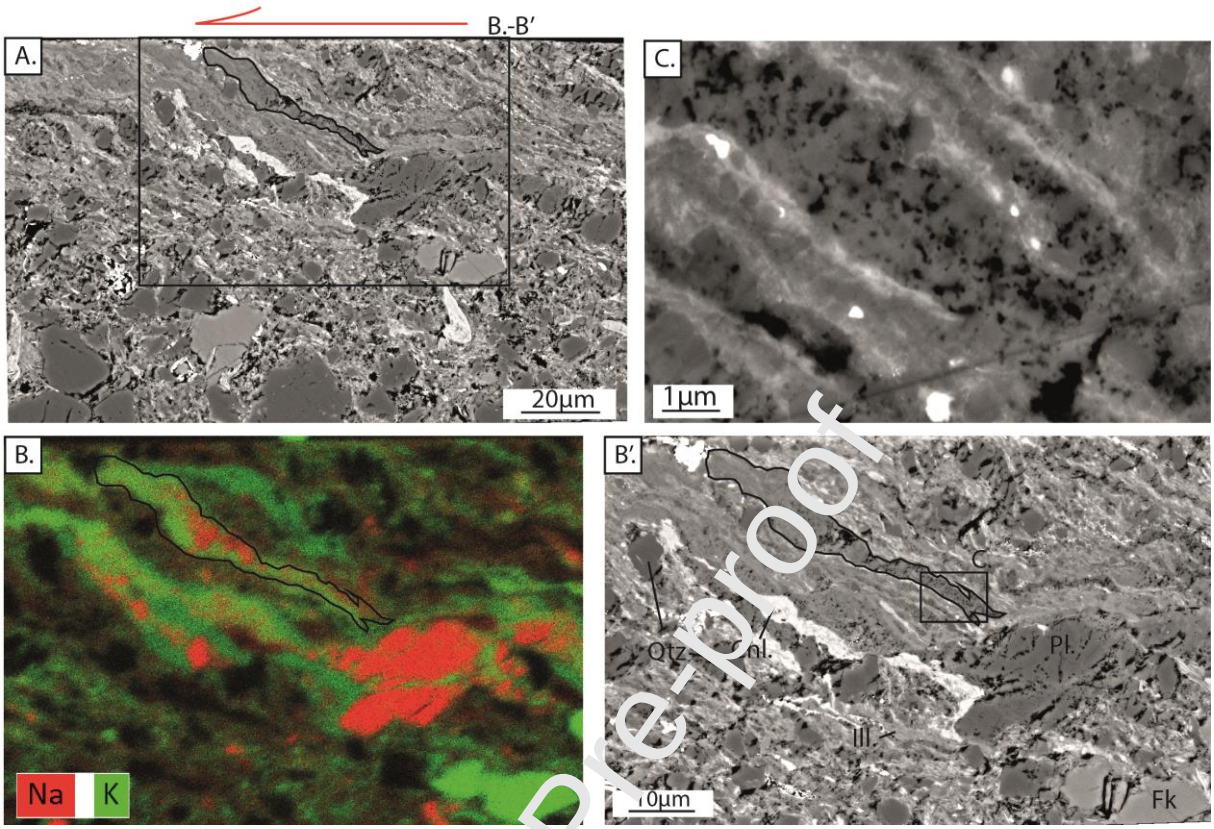

Figure 13 : A. Large-scale view showing the elongation of the different mineral phases in a high strain layer adjacent to the slip plane. Note also the increase in nanoporosity in the quartz and feldspar aggregates in the high-strain layer B.-B'. While away from the high strain layer, K-feldspar and Plagioclase have composition of pure endmember minerals, in the high-strain-zone, the comminuted feldspar have a composition involving both Na and K. C. Close-up view of the comminuted feldspar, where the very large porosity due to fragmentation is visible. A, B' and C: BSE images, B EDS map for Na and K. Sample PP64.1. In B', Qtz, Pl, Fk, Ill and Chl stand for Quartz, Plagioclase, K-feldspar, Illite and Chlorite, respectively.

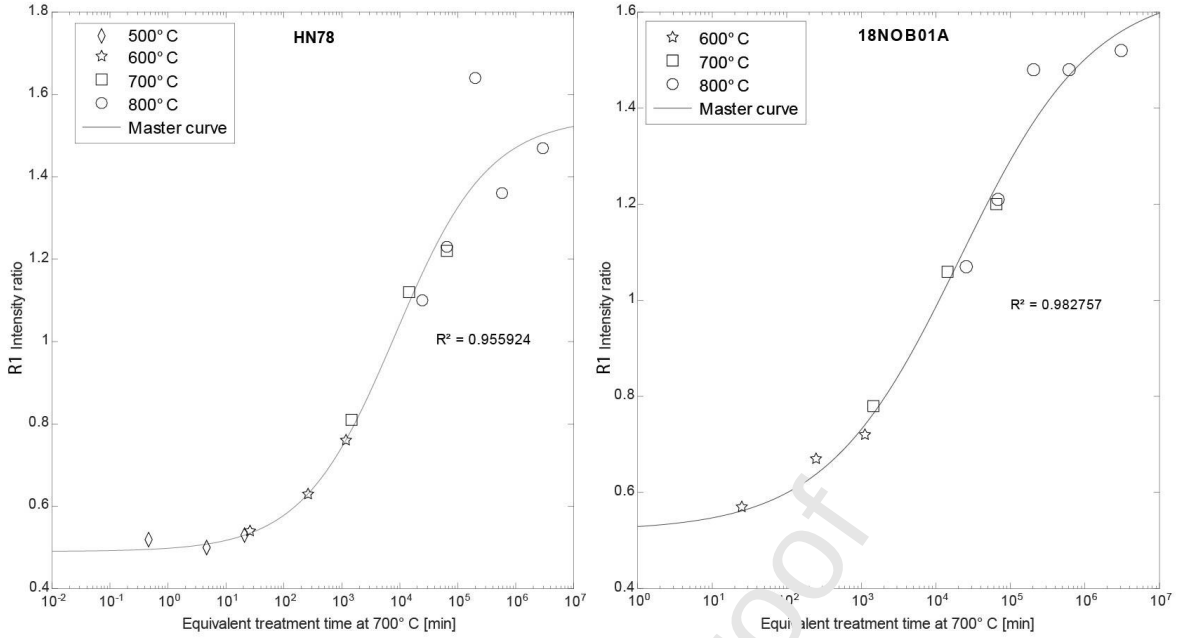

Figure 14: Master curves resulting for the superposition model for 18NOB01A **(a)** and HN78 **(b)**, following (Nakamura et al., 2017, 2020)

Table 1

Sample	*Raman spectroscopy*										*Vitrinite Reflectance*		*Rock Eval pyrolyse*
	D1 band (cm^{-1})	***D1 band FWHM***	***G band (cm^{-1})***	***G band FWHM***	***R2 ratio***	***RA1 ratio***	***R1 Intensity Ratio***	***Width ratio***	***D/G dist. (cm^{-1})***	***Estimated temperature (°C) [a]***	***Rm%***	***Estimated temperature (°C) [b]***	***Tmax***
18NOB01A	1358 ± 7	105 ± 13	1610 ± 7	69 ± 18	0.48 ± 0.09	0.47 ± 0.10	0.60 ± 0.08	1.66 ± 0.62	252 ± 7	-	0.54 ± 0.04	84 ± 7°C	437°C
HN78	1350 • ± 2	116 ± 6	1603 ± 3	52 ± 5	0.53 ± 0.01	0.53 ±0.01	0.49 ± 0.02	2.25 ±0.14	254 ± 2	201 ± 11	-	-	-

[a] Lahfid et al., 2010; [b] Barker, 1988

wt%	**Loss on ignition**	**SiO2**	**TiO2**	**Al2O3**	**FeO**	**MgO**	**MnO**	**CaO**	**Na2O**	**K2O**	**P2O5**	**SO3**
18NOB01A	4.36	64.08	0.72	16.73	5.82	1.9	0.04	0.29	1.49	3.26	0.23	0.17
HN78	8.38	58.77	0.66	14.87	4.81	2.06	0.07	4.67	1.68	2.83	0.15	0.61

Table 2

Sample	Temperature (°C)	Time (hours)	***Raman spectroscopy***																					
			D1 band (cm^{-1})	*SD*	*D1 band FWHM*	*SD*	*G band (cm^{-1})*	*SD*	*G band FWHM*	*SD*	*R2 ratio*	*SD*	*RA1 ratio*	*SD*	*R1 Intensity Ratio*	*SD*	*Width ratio*	*SD*	*D/G dist. (cm^{-1})*	*SD*	*Gss/D2 dist. (cm^{-1})*	*SD*	*Estimated temp. [a][b]*	*SD*
18NOB01A	*Starting materials*		1358.58	7.05	137.69	10.18	1610.01	7.04	68.90	0.48	1.00	0.04	0.47	0.10	0.60	0.00	1.66	0.06	252.20	7.29	259.75	0.20	-	-
	500	24	1363.60	3.14	146.08	1.10	1600.61	0.70	61.21	0.53	1.00	0.04	0.53	0.01	0.49	0.00	2.25	0.14	254.22	2.33	225.87	0.61	-	-
	500 [1]	24 [	1353.40	10.16	137.04	10.54	1610.10	7.04	68.90	0.48	1.00	0.04	0.47	0.10	0.60	0.00	1.66	0.06	252.20	7.29	259.75	0.20	-	-

	1]	5				7				0	2	0	2		2	3	2						
500	240	1354	3.0	118	5.0	1608	1.0	53	3.9	0.55	0.01	0.53	0.01	0.52	0.02	2.23	0.12	255	2.7	21.4	2.3	*201*	16.3
500	1080	1349	2.4	118	5.8	1608	0.5	49	3.6	0.58	0.01	0.55	0.01	0.52	0.02	2.42	0.09	260	2.5	19.7	3.1	*224*	13.6
600	24	1343	0.6	123	1.9	1608	0.6	49	1.4	0.62	0.01	0.57	0.01	0.57	0.01	2.51	0.10	265	0.8	19.6	1.6	*249*	9.0
600 [1]	24 [1]	1343	0.6	122	3.9	1608	0.3	48	1.4	0.61	0.01	0.57	0.01	0.58	0.02	2.51	0.05	265	0.5	19.2	1.1	*247*	10.8
600	240	1341	0.9	123	3.8	1610	2.6	48	1.2	0.67	0.01	0.61	0.01	0.67	0.02	2.54	0.07	269	2.7	17.4	0.5	*297*	9.3
600	1080	1343	0.7	116	3.6	1610	2.3	49	1.1	0.68	0.01	0.63	0.01	0.72	0.02	2.36	0.08	267	2.5	17.3	0.4	*313*	8.4
700	24	1345	1.2	118	3.6	1608	3.5	53	1.5	0.69	0.01	0.63	0.01	0.78	0.01	2.23	0.05	262	3.5	18.4	0.4	*320*	11.0
700	240	1352	1.0	98	2.5	1600	1.6	60	1.6	0.69	0.01	0.63	0.01	1.06	0.02	0.63	0.04	248	0.8	21.9	0.5	*317*	15.7
700	1080	1351	0.8	93	4.2	1597	0.9	62	2.0	0.70	0.01	0.64	0.01	1.20	0.04	3.84	0.23	246	1.1	23.0	0.6	328	4.1
800	3	1348	1.1	89	4.6	1600	6.7	54	1.9	0.68	0.03	0.65	0.01	1.07	0.05	1.65	0.10	253	7.4	20.4	1.0	337	12.6
800 [2]	3 [2]	1348	0.7	87	3.3	1598	2.5	54	1.9	0.69	0.02	0.65	0.01	1.10	0.03	1.61	0.10	250	2.9	20.4	1.7	333	8.3
800	8	1349	0.7	80	2.1	1598	3.0	54	1.3	0.69	0.02	0.65	0.01	1.21	0.04	1.48	0.06	249	2.9	21.2	0.9	333	7.1
800 [2]	8 [2]	1350	0.7	78	3.7	1597	2.0	55	1.8	0.69	0.02	0.65	0.01	1.23	0.04	1.41	0.08	247	2.2	21.8	1.0	335	7.1

	800	24	1				1				0	0	0	0		0	1	0										1
			3	0		5	5	2		1	.	.	.	.	1.	.	.	.	2	2	2	0		1
			5	.	7	.	9	.	6	.	6	0	6	0	4	0	1	0	4	.	3.	.	33	.
			1	8	0	2	6	4	0	9	9	3	5	1	8	9	7	8	4	8	3	7	6	9
	800	24																						
	0	4	1				1				0	0	0	0		0	1	0						
	[2]	[	3	0		2	5	0		1	.	.	.	.	1.	.	.	.	2	0	2	0		4
		2	5	.	7	.	9	.	5	.	6	0	6	0	3	0	2	0	4	.	3.	.	33	.
		]	2	4	3	4	7	5	9	7	9	1	4	1	9	4	4	5	5	7	9	6	4	0
	800	72	1				1				0	0	0	0		0	1	0						
			3	0		3	5	0		2	.	.	.	.	1.	.	.	.	2	1	2	0		5
			4	.	7	.	9	.	5	.	6	0	6	0	4	0	2	0	4	.	2.	.	34	.
			9	8	0	9	6	9	7	0	7	1	4	1	8	9	2	5	7	3	6	7	1	1
	800	72																						
	[2]	[	1				1				0	0	0	0		0	1	0						
		2	3	0		4	5	5		2	.	.	.	.	1.	.	.	.	2	5	2	1		6
		]	4	.	7	.	9	.	5	.	6	0	6	0	2	0	3	0	5	.	1.	.	33	.
			9	9	8	6	9	3	9	2	8	1	4	1	9	6	3	9	0	6	9	0	9	6
	800	36	1				1				0	0	0	0		0	1	0						
	0	0	3	0		4	5	5		2	.	.	.	.	1.	.	.	.	2	5	2	1		5
			5	.	6	.	9	.	6	.	6	0	6	0	5	0	0	0	4	.	4.	.	34	.
			1	7	9	3	9	6	5	6	7	1	3	1	2	9	6	5	8	8	4	0	1	6
	800	36																						
	0	0																						
	[2]	[	1				1				0	0	0	0		0	1	0						
		2	3	0		3	5	5		2	.	.	.	.	1.	.	.	.	2	5	2	1		4
		]	5	.	7	.	9	.	6	.	6	0	6	0	4	0	0	0	4	.	4.	.	34	.
			2	5	2	4	8	1	6	3	8	1	3	1	9	9	9	6	6	1	3	0	1	2
	Starting		1				1				0	0	0	0		0	2	0						1
H	*material*		3	2	1	6	6	3		5	.	.	.	.	0.	.	.	.	2	2	2	0		1
N7	*s*		5	.	1	.	0	.	5	.	5	0	5	0	4	0	2	1	5	.	1.	.	*20*	.
8			0	0	6	0	3	0	2	0	3	1	3	1	9	2	5	4	4	0	4	9	*1*	0
	500	24	1				1				0	0	0	0		0	2	0						2
			3	1	1	3	6	0		2	.	.	.	.	0.	.	.	.	2	1	2	1		0
			5	.	1	.	0	.	5	.	5	0	5	0	5	0	2	0	5	.	3.	.	*17*	.
			0	0	5	2	3	6	2	0	4	2	2	2	2	2	1	7	7	1	1	4	*8*	8
	500	24	1				1				0	0	0	0		0	2	0						1
			3	1	1	2	6	0		1	.	.	.	.	0.	.	.	.	2	1	1	1		6
			5	.	1	.	0	.	4	.	5	0	5	0	5	0	4	0	5	.	8.	.	*21*	.
			0	4	2	0	8	3	6	2	6	1	5	1	0	2	3	5	9	3	6	3	*3*	8
	501	10	1				1				0	0	0	0		0	2	0						2
	0	08	3	2	1	5	6	0		4	.	.	.	.	0.	.	.	.	2	2	1	2		4
			4	.	1	.	0	.	4	.	5	0	5	0	5	0	4	1	6	.	9.	.	*23*	.
		0	9	6	9	3	8	5	9	3	8	1	6	2	3	2	7	4	0	8	3	3	*0*	6
	600	24	1				1				0	0	0	0		0	2	0						
	0	4	3	0	1	0	6	5		1	.	.	.	.	0.	.	.	.	2	0	1	0		9
			4	.	1	.	0	.	4	.	6	0	5	0	5	0	6	0	6	.	6.	.	*25*	.
			2	8	5	5	8	0	4	0	1	1	8	1	4	2	0	2	6	7	3	7	*4*	8
	600	24																						
	0	4	1				1				0	0	0	0		0	2	1						2
	[1]	[	3	3	1	7	6	4		4	.	.	.	.	0.	.	.	.	2	1	2	2		4
		1	4	.	2	.	0	.	5	.	6	0	5	0	5	0	4	1	6	.	0.	.	*24*	.
		]	0	6	6	5	5	1	2	2	2	2	8	2	9	3	4	6	4	2	7	3	*6*	4
	600	24	1	0	1	4	1	3	4	1	0	0	0	0	0.	0	2	0	2	3	1	0	*29*	1
	0	4	3	.	1	.	6	.	5	.	.	.	.	.	6	.	.	.	6	.	6.	.	*9*	4

	0	4	9	4	1	0	4		1	6	0	6	0	3	0	5	0	9	3	6	3		.
		0				9				6	1	1	1		2	1	7						9
60	1	1				1				0	0	0	0		0	2	0						1
0	0	3	1	1	5	6	3		1	.	.	.	.	0.	.	.	.	2	3	1	0		6
	8	4	.	0	.	0	.	4	.	6	0	6	0	7	0	9	0	6	.	7.	.	*32*	.
	0	2	0	7	1	4	8	7	7	8	1	3	1	6	2	2	9	3	9	0	5	*1*	6
70	2	1				1				0	0	0	0		0	2	0						1
0	4	3	1	1	4	6	3		2	.	.	.	.	0.	.	.	.	2	4	1	0		0
		4	.	0	.	0	.	5	.	6	0	6	0	8	0	1	1	6	.	8.	.	*33*	.
		4	1	9	1	5	8	0	2	9	1	5	2	1	2	8	0	1	5	0	7	*2*	9
70	2	1				1				0	0	0	0		0	1	0						1
0	4	3	0		3	6	1		1	.	.	.	.	1.	.	.	.	2	1	2	0		3
	0	5	.	9	.	0	.	6	.	7	0	6	0	1	0	5	0	4	.	1.	.	*33*	.
		2	8	4	7	0	0	0	9	0	1	4	1	2	4	8	5	8	0	7	7	*3*	4
70	1	1				1				0	0	0	0		0	3	0						
0	0	3	0		3	5	4		2	.	.	.	.	1.	.	.	.	2	4	2	1		6
	8	5	.	8	.	9	.	6	.	7	0	6	0	2	0	8	3	4	.	3.	.	33	.
	0	2	8	8	4	8	2	0	5	0	1	4	1	2	4	7	4	6	5	2	3	0	0
80	3	1				1				0	0	0	0		0	1	0						
0		3	0		2	6	3		1	.	.	.	.	1.	.	.	.	2	4	2	1		5
		4	.	8	.	0	.	5	.	7	0	6	0	1	0	6	0	5	.	0.	.	32	.
		8	7	5	1	0	8	0	7	0	1	7	1	0	3	9	7	2	1	0	1	9	5
80	3	1				1				0	0	0	0		0	1	0						
0	[	3	0		3	5	1		1	.	.	.	.	1.	.	.	.	2	0	2	0		2
[2]	2	4	.	8	.	9	.	5	.	7	4	6	0	1	0	6	0	5	.	0.	.	32	.
	]	9	6	4	1	9	0	1	7	1	1	7	0	3	3	4	4	0	9	3	4	6	4
80	8	1				1				0	0	0	0		0	1	0						
0		3	1		3	5	4		2	.	.	.	.	1.	.	.	.	2	4	2	1		8
		5	.	8	.	9	.	5	.	7	0	6	0	2	0	4	0	4	.	1.	.	33	.
		0	0	3	9	8	2	7	4	0	2	5	1	3	4	5	8	8	5	9	2	0	0
80	8	1				1				0	0	0	0		0	1	0						
0	[	3	0		1	5	1		1	.	.	.	.	1.	.	.	.	2	1	2	0		3
[2]	2	5	.	7	.	9	.	5	.	7	0	6	0	2	0	5	0	4	.	1.	.	32	.
	]	0	4	9	8	2	1	3	5	1	1	7	1	5	3	0	4	9	1	0	5	7	4
80	2	1				1				0	0	0	0		0	1	0						
0	4	3	0		3	5	0		2	.	.	.	.	1.	.	.	.	2	1	2	0		6
		5	.	9	.	9	.	5	.	6	0	6	0	6	0	1	0	4	.	2.	.	33	.
		0	9	1	1	7	9	2	1	9	1	9	1	4	9	7	7	7	0	8	9	3	6
80	2																						
0	4	1				1				0	0	0	0		0	1	0						
[2]	[	3	0		1	5	0		1	.	.	.	.	1.	.	.	.	2	0	2	0		3
	2	5	.	7	.	9	.	5	.	7	0	6	0	4	0	2	0	4	.	2.	.	32	.
	]	2	7	2	4	7	5	7	7	2	1	7	1	9	5	7	3	5	8	8	5	0	2
80	7	1				1				0	0	0	0			1	0						
0	2	3	1		6	5	3		2	.	.	.	.	1.	0	.	.	2	3	2	0		9
		5	.	7	.	9	.	6	.	6	0	6	0	3	.	2	1	4	.	3.	.	33	.
		2	4	6	6	6	2	1	4	9	2	5	1	6	1	6	2	4	1	5	8	3	5
80	7																						
0	2	1				1				0	0	0	0		0	1							
[2]	[	3	1		4	5	3		3	.	.	.	.	1.	.	.	0	2	4	2	1		9
	2	5	.	7	.	9	.	5	.	6	0	6	0	3	0	2	.	4	.	3.	.	33	.
	]	1	2	6	7	7	8	9	1	8	2	5	1	1	5	8	1	6	5	2	1	8	6
80	3	1	1		2	1	3		2	0	0	0	0	1.	0	1	0	2	3	2	0		5
0	6	3	.	7	.	5	.	6	.	.	.	.	.	4	.	.	.	4	.	6.	.	33	.
	0	5	2	6	4	9	5	8	8	6	0	6	0	7	0	1	0	2	3	1	8	4	3

			3				6				9	1	4	1		7	1	5													
80 0 [2]	3 6 0 [2]		1 3 5 2	0 . 0 9	6 8	3 . 1	1 5 9 6	4 . 2	6 4	2 . 2 8	0 . 7 0	0 . 0 2	0 . 0 6	0 . 0 2	1. 6 1	0 . 0 9	1 . 0 7	0 . 0 3	2 4 3	4 . 5	2 5. 7	1 . 1	33 1	9 . 1
[1] wet: addition of 2 wt% H2O; [2] wet: addition of 10 wt% H2O																															
[a] Lahfid et al., 201; [b] Beyssac et al., 2002																															

Table 3

Experiments	Name	Deformation mode	Pistons	Duration	Temperature	Confining pressure	Type of material	Final height (mm) for coaxial experiments, final thickness (mm	Initial assembly diameter (mm)	Displacement rate	Total displacement	Stick-slip	Ss. displ.	Stress drop	Peak differential stress (before stick-slip if occurred)	Conditions of pore fluid	Deformation microstructures	Raman Results

								) for shear experiments									
Paterson Rig	PP629	Shear	Porous alumina	5 hours	700C	50 MPa	Powder	0.8	15	0.1 μm.s^{-1}	1.4 mm	No	-	-	320 MPa	Pore fluid connected with water, kept at a low pressure	Compaction only (dehydration of clay made the sample more compact than	None

																	the alumina pistons, which localized the deformation)	
	PP630	Shear	Porous alumina	6 hours	700° C	150 MPa	Powder	1.6	15	0.1 μm.s^{-1}	3.5 mm	No	-	-	380 MPa	Pore fluid connected with water, kept at a low	Compaction only (dehydration of clay made the sa	None

															pressure	mple more compact than the alumina pistons, which localized the deformation)	
	PP632	Shear	Non-porous alu	7 hours	700° C	150 MPa	Powder	1.7	15	0.1 µm.s^{-1}	3.5 mm	Yes	27 µm/15 µm	40 MPa/20 MP	66 MPa/43 MPa	No control of pore fluid pr	Vitreous slip plane along	IR 0.691 ± 0.029 in the hos

			mina											a		essure	piston	trock, 0.719 ± 0.064 along the slip surface (+4 %)
	PP633	Shear	Non-porous alumina	4 hours	700° C	150 MPa	Powder	1.8	15	0.05 µm.s^{-1}	1.0 mm	Yes	45 µm	30 MPa	64 MPa	No control of pore fluid pressure	Breciazones (~200 µm-thick, with heterogeneous gra	0.656 +/- 0.012 in the host rock, 0.673 +/- 0.015 (m

																	incommination, large porosity) variously distributed within the sample + Vitreous slip plane (could not	axvalue), i.e. +2.6% increase in brecciated layer along the slip plane

																be observed with SEM) along piston	
	PP636	Shear	Non-porous aluminia, roughened contact	6 hours	70 °C	150 MPa	Powder	2.1	15	0.05 µm.s^{-1}	1.6 mm	Yes	90 µm	50 MPa	128 MPa	No control of pore fluid pressure	High strain layer (~1 µm-thick, ultrafine-grained, no porosity) and shear	0.784 +/- 0.05 in the 1 µm-thick high strain layer, 0.726 +/- 0.03 in ~20

			plane														ed zone (~10-20 µm-thick, with remaining clasts and aligned clays) along piston	µm-thick the foliated layer, 0.673+/-0.02 in the undeformed host rock

	PP638	Co-axial	Non-porous alumina	7 hours	700° C	150 MPa	Intact	24	15	0.1 μm.s^{-1}	2.6 mm	Yes	60 μm	50 to 60 MPa	127 MPa	No control of pore fluid pressure	Conjugate slip planes, along which brecciated zones are locally visible, and accompanied by larger zone	0.707 +/- 0.028; No difference between host rock and brecciated zones

																where the porosity is decreased	
	PP641	Co-axial	Non-porous alumina	42 hours	600°C	150 MPa	Intact	31	15	0.015 $\mu m.s^{-1}$	3.0 mm	Yes	110 µm	135 MPa	181 MPa	No control of pore fluid pressure	Conjugate shear-zones (~50µm-thick) + slip plane	0.624 +/- 0.017 in the undeformed zone, 0.79 +/- 0.051 in the shear

																	zone: +14% increase in the shear zone
	PP649	Co-axial	Non-porous alumina	72 hours	600°C	150 MPa	Intact	29	15	Constant load: four steps at 115, 130, 140 and 155 MPa	2.3 mm	No	-	-	-	No control of pore fluid pressure	Homogeneous shortening	IR 0.622+/-0.025 in the whole sample

Experiments	Name	Deformation mode	Apparatus	Type of displacement	Time	Temperature	Type of material	Pressure	Peak stress	Applied nominal load	Displacement	Strain rate	Gamma	Pt-jacket structure	Localized def.	Deformation microstructures	Raman Results
Solid medium Grigs type apparatus	T609BM	Shear	Tullis-modified	Constant strain rate	34 hours	600° C	Intact	1000 MPa	350 MPa	-	1.5 mm	$2.57E10^{-5}$ s^{-1}	3.1	No	Yes	Micro-breccia, with increased porosity, 20 to 50 µm-thick, along	IR 0.831+/-0.67; No difference between undeformed and brecciated zone; large gradients in IR betwe

															the slip plane. No visible foliated shear zone	en upper and lower pistons: 0.804+/-0.082 for top part vs. 1.013+/-0.075 for bottom part
	T610BM	Shear	Tullis-modified	Constant strain rate	72 hours	400° C	Intact	1000 MPa	950 MPa	-	2.3 mm	$2.24E10^{-5}$ s^{-1}	3.0	Yes	Yes	Micro-breccia, with increased porosity, along th	IR 0.586+/-0.037 No difference between undeformed, brecciated and shear zone

															e main slip plane. 10 to 30 µm-thick shear zone with deflected clays near the slip plane. Foliation well de	

															veloped in broad zones around the slip plane.	
	OR87BM	Shear	Newgeneration	Constantload	17.5 hours	600°C	Intact	1000 MPa	-	200, 300, 400 and 500 MPa	3.1 mm	$9.9E10^{-6}$ s^{-1} (for 5000 MPa)	5.3	No	Yes	S-Cductile structures + a main slip plane is present; mo	IR 0.719+/-0.035 in the undeformed zone, IR 0.858 +/-0.058 in the high strain zon

																stly brecciaalong slip plane + few µm-thick strongly sheared zone along the slip plane	e : +19 % increase in the shear zones

	OR92BM	Shear	Newgeneration	Constantload	20hours	600°C	Intact	1000MPa	-	500Mpa	8.1mm	5.0E10^{-4} s^{-1}	16	Yes	Yes	Amainsliplane,accompaniedbyshearzones(~100µmthick)+stronglyshearedzone(~30µm-thick,very	IR0.692+/-0.028inthedeformedzone,IR0.979+/-0.036inthehighstrainzone:+41%increase

																strong grain-size reduction, no porosity) + brecciazone (along the slip interface?) + Brecciazones alo	

																ng sec on da ry sli p pla ne s	

Table 4

	HN78	18NOB01A
$R1_{min}$	0.49	0.52
$R1_{max}$	1.5450	1.6523
h	0.5407	0.4847
m	-1.6733 x 10^4	-2.1392 x 10^4
ln A	-15.791	-21.339

Table 5

Reference	Type of occurrence	Deformed material	Organic matter analyzed	Type of structure of deformation	Initial maturity of organic matter	Range of organic matter evolution (in terms of Raman signal)	Method of observation	Evolution of organic matter properties in strain zones (qualitative)	Evolution of organic matter properties in strain zones (quantitative)	Delta crystallographic ordering in strain zone	Effect of local heat pulse
Savage et al. 2014	Natural	Shales	Organic compounds in the rock	Kodiak pseudotachylyte, Alaska, US	220-270° C (Rajic et al., 2023)	Carbonization	Gas chromatography-mass spectroscopy on extract	-	Increase in the proportion of diamondoids/n-alkanes (=increased	Positive	Inferred by the authors

							ed organic molecules		maturation)		
Savage et al. 2019	Natural	Sandstones	All organic compounds in the rock	Punchbowl strike-slip fault, US	Less than 120° C of maximum temperature of burial (Polissar et al. 2011)	Carbonization	Gas chromatography-mass spectroscopy on extracted organic molecules		Methylphenanthrene isomers ratio MPI-4 increase in principal slip zone	Positive	Inferred by the authors
Muirhead et al. 2021	Natural	shales and phyllites	CM particles	Fault zones in various sedimentary terranes	Variable, from low grade to greenschist-facies conditions	Carbonization	RSCM		Inconsistent evolution: either increase or decrease in R1	Non systematic	possible
Kedar et al. 2020	Natural	marls	CM particles	Large-scale folding	sub-greenschist facies	Carbonization to graphitization	RSCM		Decrease in R1 in the overturned limb of a fold	Positive	Not inferred by the authors; the sole effect of deformation is invok

											ed
Ito et al. 2017	Natural	shales	CM particles	Pseudotachylyte in the Shimanto Belt, Japan (Mugi mélange)	T~160°C (Raimbourg et al. 2019)	Carbonization	RSCM		Increase in ID1/ID2	Positive	Inferred by the authors
Kaneki et al., 2016	Natural	Turbidites	CM particles extracted from the rock	Pseudotachylyte in the Shimanto Belt, Japan (Nonokawa formation)	~210-230°C (Raimbourg et al. 2019)	Carbonization	RSCM	Decrease in the intensity of IR signal of C-H and aromatic C-C signal in deformed zone compared to host rock	Slight Increase in ID1/ID2, although the spectra are noisy	Positive	Inferred by the authors
Ujiie et al. 2021	Natural	Pelagic mudstones	CM particles	pseudotachylyte and ultracataclasite	~220°C	Carbonization	RSCM		Increase in ID1/ID2	Positive	Inferred by the authors
Suchy et al. 1997	Natural	limestones, marls and greywack	Vitrinite	Greenschist-facies shear zones	250-350°C (RSCM Girault et al.	Graphitization	Optical microscopy + vitrinite reflectance	Graphitization of vitrinite particles in plasti	-	Positive	Inferred by the authors

		es			2020)			c strain zones			
Petroccia et al. 2022	Natural	Quartzites and phyllites	CM particles	Shear zones in the Variscan Belt in Sardinia, Italy	420-520° C	Graphitization	RSCM		Decrease in R2 from undeformed to the core of the shear zone	Positive	Inferred by the authors
Nakamura et al. 2015	Natural	Biotite-muscovite schists	CM particles	Cataclasites, ultracataclasites and pseudotachylytes in the Hidaka Metamorphic Belt, Japan	340-600° C	Graphitization	RSCM + HRTEM		Increase in R2 in zones of brittle deformation	Negative	Not inferred by the authors; the sole effect of deformation is invoked

Reference	Type of occurrence	Deformed material	Organic matter analyzed	Type of structure of deformation	Initial maturity of organic matter	Range of organic matter evolution (in terms of Raman signal)	Method of observation	Evolution of organic matter properties in strain zones (qualitative)	Evolution of organic matter properties in strain zones (quantitative)	Delta maturation in strain zone	Effect of local heat pulse	Experimental conditions

Savage et al. 2018	High velocity friction experiments (~m/s)	Woodford Shale, from central Oklahoma	Organic compounds in the rock	Principal slip zone of ~200µm of thickness	Relatively immature	Carbonization	Gas chromatography-mass spectroscopy on extracted organic molecules	?	methylphenanthrene isomers ratio MPI-4 increase (=increase in maturity) in principal slip zone, as a function of work density and power density	Positive	yes	5 to 10MPa normal stress, water-saturated conditions at room temperature
Kirilova et al. 2017	Medium velocity friction experiments (~1 to 100 µm/s)	Compacted and heated graphite powder	Graphite particles	Principal slip zone, compacted near the slip surface, with higher porosity away from it	Graphite powder	Graphitization	RSCM	?	Increase in R2 in zones of brittle deformation	Negative	?	5 to 25MPa normal stress, room temperature and room humidity
Kaneki and Hirono, 2019	High velocity friction experiments (~m/s)	CM powder	CM particles	Homogeneous deformation, without description of the micros	Variable, from low grade CM to graphite	Variable	RSCM + HRTEM + IR	?	Increase in R1 for low to intermediate maturity CM, decrase in R1 for graphite	Positive in low to intermediate maturity CM, nega	yes	normal stresses of 0.5, 1.0, 1.5 and 2.0 MPa, slip rate

				tructures of deformation						tive in graphite		of 1 m/s and slip distance of 15 m under water-saturated conditions at room temperature
Ito et al. 2017	High velocity friction experiments (~m/s)	Natural shales	CM particles	Grain comminution and melting within a pseudotachylyte layer	Low-grade (T<150°C)	Carbonization	RSCM	?	Increase in ID1/ID2	Positive	yes	2.7 to 13.3 MPa normal stress, room temperature and humidity
Furuichi et al. 2015	High (~m/s) and low (0.15 mm/s) velocity friction experiments	Hemipelagic mudstone from the Nankai Trough artificially mixed with low	CM particles	Relatively thick foliated zone in wet tests, principal slip zone in dry tests at low and high velocit	Very low grade - modern sediments at max ~1kmbsf	Carbonization	RSCM	?	Increase in ID1/ID2 in high velocity friction experiments, no change in low velocity friction experiments	Positive	yes	Dry and wet tests were conducted at a slip rate of 1.3 m/s and a normal stress (σn)

		grade brown coal from the Kumano Basin		y								of 2.0 MPa with displacement of ~11 m. In addition, one dry test was performed at a low slip rate of 0.15 mm/s and low σ_n of 1.0MPa with displacement of ~0.3 m
Aubry et al. 2018	Tri-axial deformation test, with stick-slip events on a fracture plane	Westerly granite with a saw-cut fracture plane	Carbone coating on the fracture plane	Fault plane with molten surface	?	Carbonization	RSCM	?	Increase in R1 in strained samples	Positive	yes	Room temperature, confining pressure of 45, 90 and 180MPa, displacement rate

												of 3µm/s
Bustin et al. 1995	Griggs-type HPHT shear and coaxial experiments	Anthracite coal from Pennsylvania and a high volatile bituminous coal from Nova Scotia.	idem	?	Low grade	Carbonization then graphitization	TEM+XRD+Raman	XRD and TEM show an evolution in strained samples towards a graphite-like structure	Increase in R1 in strained samples	Positive	no	Confining pressures of 0.6, 0.8 or 1.0 GPa, temperatures between 400° C and 900° C, strain rates of 10^{-5}/s or 10^{-6}/s
Oohashi et al. 2011	Rotary shear experiments, 50 mm/s to 1.3 m/s	Powders of commercial amorphous carbon	idem	Principal slip zone of ~50µm thickness	Amorphous	-	XRD+TEM	XRD and TEM show an evolution in strained samples towards a graphite-like structure, only in	?	Positive	yes	Normal stresses of 0.5 to 2.8 MPa, equivalent slip rates (Ve) of 50 mm/s to 1.3 m/s, and displacements of 0.09

								high-velocity and under N2 atmosphere experiments				to 118 m. Atmosphere of N2 or of air
Kuo et al., 2017	Rotary shear experiments, 0.0003 m/s (subseismic) and 3 m/s (seismic)	Fault breccia from the Longmenshan fault zone	CM particles	Principal slip zone of ~200 µm of thickness	T~350°C (from the absence of D2, see Kouketsou et al. 2014)	Graphitization	Raman +TEM	TEM shows the crystallization of graphite particles only in experiments at fast velocity and without added water	Decrease in R1, for slow and fast slip, irrespective of water saturation level	Positive	yes	Normal stresses of 8.5 MPa, slip rates of 0,3 mm/s and 3 m/s, and displacements of 3 m, at room temperature and humidity and, by the addition of 0.5 g of distilled water, at water-dampened

												conditions
Kaneki and Hirono, 2018	Rotary shear experiments, slip rate of 0.001 m/s + subsequent heating under N2 or vacuum	Mixture of quartz and lignite powder	CM particles	?	Immature type-II kerogen	Carbonization	RSCM + IR	Decrease in aliphatic and aromatic C-C bonds as a result of shear only	No decipherable Raman spectrum as a result of shear only	Positive	?	Room humidity, equivalent slip rate of 0.001 $m.s^{-1}$ (Hirose & Shimamoto, 2005), 10m of total displacement at normal stresses of 1 and 3 MPa under air condition.

Author Contribution

Benjamin Moris-Muttoni: Conceptualization, Investigation, Writing - original draft, Acquisition, Analysis and interpretation of Raman spectra

Hugues Raimbourg: Conceptualization, Writing - original draft, Supervision;

Rémi Champallier: Experiments

Romain Augier: Interpretation of Raman spectra

Abdeltif Lahfid: Interpretation of Raman spectra

Emmanuel Le Trong: Numerical modelling

Ida Di Carlo: SEM imaging

Declaration of interests

The authors declare the following financial interests/personal relationships which may be considered as potential competing interests:
Hugues Raimbourg reports financial support was provided by French National Research Agency.

Highlights

- Using Raman we studied carbonaceous matter (CM) evolution with strain and temperature
- Kinetics of evolution were derived from high-pressure experiments of static heating
- High-pressure deformation experiments show the large effect of strain on Raman of CM
- Raman anomalies in natural fault zones can result from strain and not temperature